TECHNICAL MEMORANDUM

594

The nonhydrostatic global IFS/ARPEGE: model formulation and testing

Nils P. Wedi, Karim Yessad and Agathe Untch

Research Department

October 2009

European Centre for Medium-Range Weather Forecasts
Europäisches Zentrum für mittelfristige Wettervorhersage
Centre européen pour les prévisions météorologiques à moyen terme

Abstract

In preparation for global applications at horizontal scales finer than about 10 km, where nonhydrostatic dynamics becomes important, the efficacy and stability of the nonhydrostatic model developed by the AL-ADIN group and made available by Météo-France in the global IFS/ARPEGE model are assessed. The main attraction of this nonhydrostatic dynamical core is its algorithmic similarity to the existing hydrostatic IFS (H-IFS). The performance of the nonhydrostatic model (NH-IFS) is assessed for a wide range of scales and for a set of canonical test cases relevant to atmospheric flows. The results obtained for a range of idealised nonhydrostatic flow problems compare satisfactorily to Cartesian-domain analytic solutions, where available, and to the nonhydrostatic research code EULAG. At hydrostatic scales (for grid-sizes upto 10 km) the NH-IFS gives very similar forecasts to the operational hydrostatic IFS, and can be run stably with the rather long timesteps used with the latter model. However, the computational cost of the NH-IFS per timestep is substantially larger than with the H-IFS (double at 10 km resolution). It is concluded that the NH-IFS dynamical core is a possible choice for future, globally-uniform high resolution applications at ECMWF, provided its cost can be reduced.

1   Introduction

The Centre plans to implement a horizontal resolution of 10 km by 2015 for its assimilation and deterministic forecast system, beyond which a nonhydrostatic dynamical core will be required. The current dynamical core of the IFS model is based on the hydrostatic primitive equations and is likely to be of limited use at horizontal resolutions finer than about 10 km, where non-hydrostatic effects will become important. (ECMWF, 2000; Wedi and Smolarkiewicz, 2009). Rather than developing such a dynamical core for the Centres model from scratch or investigate other existing formulations it was decided to evaluate whether the nonhydrostatic formulation developed by the ALADIN group (Bubnová et al., 1995), (ALADIN, 1997) and made available by Météo-France in the global IFS/ARPEGE model (Yessad, 2008) is able to fulfil the requirements of high accuracy, efficiency and robustness imposed by ECMWFs various global operational applications and has the potential to form the basis of the Centre's future nonhydrostatic dynamical core. This report presents the various tests performed during this assessment, discusses the results and draws some provisional conclusions.

The assessment addresses the following questions:

1.) How does the nonhydrostatic model compare in terms of robustness, accuracy and computational cost with the Centre's successful hydrostatic IFS model (H-IFS) in the hydrostatic regime?

2.) How accurately does it handle nonhydrostatic effects when these are resolved and how stable is it numerically when run at such ultra high horizontal resolutions?

Since the finest horizontal resolution at which the (global) IFS can be run to date (T2047, grid mesh of 10 km) is still too coarse to resolve nonhydrostatic phenomena, a testbed has been developed that enables testing of the global nonhydrostatic dynamical core at nonhydrostatic scales at an affordable computational cost. Rather than create a 2D vertical slice model of the 3D global model as in e.g. Hundertmark and Reich (2007) or develop a limited area version of the IFS, a testing framework more suited for the global code was developed. It is based on the idea of shrinking the radius of the planet such, that with an affordable number of grid-points covering the globe, the desired resolution resolving nonhydrostatic phenomena is achieved, but without incurring the prohibitive cost associated with such a fine resolution on the full-sized planet (Smolarkiewicz et al., 1999; Kuang et al., 2005; Wedi and Smolarkiewicz, 2009). The size of the computational domain is reduced without changing the depth or the vertical structure of the atmosphere. The underlying assumption is that the essential flow characteristics remain unchanged when the separation of horizontal and vertical scales is reduced (Kuang et al., 2005). A number of test cases from the literature, designed to test the handling of various nonhydrostatic phenomena have been adapted to the reduced-size planet testbed; see Wedi and Smolarkiewicz (2009)

for details.The results of the global nonhydrostatic IFS (NH-IFS) are compared with numerical solutions of the multi-scale anelastic research code EULAG (Prusa et al., 2008) and against LES benchmarks of limited-area models and Cartesian-domain analytic solutions where such solutions exist.

This report is organised as follows. The next section summarises the set of prognostic and diagnostic equations on which the nonhydrostatic model is based and outlines the discretisation and numerical solution procedure. Section 3 shows results from the various test cases run at different scales, summarises the performance of the NH-IFS in medium-range and seasonal forecasting at various resolutions and discusses its numerical stability as well as the computational cost. Discussions and conclusions are given section 4.

2 Model formulation

The evolution equations of the IFS are cast in a terrain following mass-based coordinate

$$\pi = A(\eta) + B(\eta)\pi_s(\lambda, \phi, t), \tag{1}$$

where $A(\eta)$, $B(\eta)$ define a set of constants and η denotes the hybrid vertical coordinate; π_s is the surface value of the vertical coordinate π (Laprise, 1992) and is equivalent to hydrostatic surface pressure in a shallow, vertically unbounded, planetary atmosphere. The temporal evolution of π_s is obtained by vertically integrating the continuity equation as

$$\frac{\partial \pi_s}{\partial t} = -\int_0^1 \nabla_\eta \cdot (m\mathbf{v}_h) d\eta, \tag{2}$$

where $\mathbf{v}_h$ denotes the horizontal velocity vector and ∇_η indicates the gradient on a constant η-surface. The vertical metric factor is defined as $m \equiv \partial\pi/\partial\eta$. The remaining prognostic equations of the IFS dynamical core were derived under the philosophy of gradually extending the hydrostatic shallow-atmosphere equations to the fully compressible Euler equations (Ritchie et al., 1995; Laprise, 1992; Bubnová et al., 1995; Temperton et al., 2001; Bénard et al., 2005; Yessad, 2008; Bénard et al., 2009), and they can be summarised as

$$
\begin{aligned}
\frac{d\mathbf{v}_h}{dt} &= -\frac{RT}{p}\nabla_\eta p - \frac{1}{m}\frac{\partial p}{\partial \eta}\nabla_\eta \Phi - 2\Omega \times \mathbf{v}_h + P_{\mathbf{v}}, \\
\frac{d\mathscr{D}}{dt} &= d(\nabla_\eta \cdot \mathbf{v}_h - D_3) - \frac{gp}{mR_dT}\left(\frac{\partial}{\partial \eta}\left(\frac{g}{m}\frac{\partial(p-\pi)}{\partial \eta}\right) - \nabla_\eta w \cdot \frac{\partial \mathbf{v}_h}{\partial \eta}\right) + \frac{d\mathscr{X}}{dt} - \frac{gp}{mR_dT}\frac{\partial P_w}{\partial \eta}, \\
\frac{dT}{dt} &= -\frac{RT}{c_V}D_3 + P_T, \\
\frac{d\mathscr{Q}}{dt} &= -\frac{c_p}{c_V}D_3 - \frac{1}{\pi}\frac{d\pi}{dt} + P_p, \\
\frac{dq}{dt} &= P_q, \\
\frac{dq_k}{dt} &= P_{q_k}.
\end{aligned}
\tag{3}
$$

Here T, p, Φ are temperature, pressure, and geopotential; $D_3 \equiv \nabla \cdot \mathbf{v}$ denotes the three-dimensional divergence; $R = R_d + (R_V - R_d)q - \sum_k R_d q_k$ is the specific gas constant of the multiphase air mixture with the gas constants of water vapour R_V and dry air R_d; q is the specific humidity and q_k symbolises other constituents, such as cloud liquid water and ice. The specific heat constants of the air mixture at constant pressure and at constant volume are c_p and c_V, respectively [1], g is the gravitational acceleration, Ω the angular velocity vector of the planetary

---

[1]Since these values are not constant in time or space in the general case, one may consider an alternative form of the equations, where c_p and c_V are included into the advection operator (Catry et al., 2007).

rotation and $P_{\mathbf{v}}, P_w, P_T, P_p, P_q, P_{q_k}$ symbolise physical forcings. In the current form of the model the pressure equation is approximated by setting $P_p = 0$. Two equations and two prognostic variables are added when the hydrostatic approximation is relaxed. The two new prognostic variables are: pressure departure $\mathcal{Q} \equiv \log(p/\pi)$ and $\mathcal{D} \equiv d + \mathcal{X}$, where d denotes the vertical divergence defined as $d \equiv -g(p/mR_dT)\partial w/\partial \eta$, with w denoting vertical velocity, and where $\mathcal{X}$, the residual, is given by $\mathcal{X} \equiv (p/RTm)\nabla_\eta \Phi \cdot \partial \mathbf{v}_h/\partial \eta$. With these variables the three-dimensional divergence is given as $D_3 = \nabla_\eta \cdot \mathbf{v}_h + \mathcal{X} + (R_d/R)d$. The total derivative of the residual $\mathcal{X}$ in (3) is evaluated along a semi-Lagrangian trajectory (Bénard et al., 2005, 2009). These particular choices for the new prognostic variables $\mathcal{Q}$ and $\mathcal{D}$ have aided the construction of a stable semi-implicit scheme of the elastic equations, see Bénard et al. (2004, 2005, 2009) for a discussion. The system of prognostic equations (2) and (3) is completed by the following diagnostic relations:

$$
\begin{aligned}
\Phi &= \Phi_s + \int_\eta^1 \frac{mRT}{\pi} e^{-\mathcal{Q}} d\eta, \\
m\frac{d\eta}{dt} &= B(\eta) \int_0^1 \nabla_\eta(m\mathbf{v}_h) d\eta - \int_0^\eta \nabla_\eta \cdot (m\mathbf{v}_h) d\eta, \\
\frac{d\pi}{dt} &= \mathbf{v}_h \cdot \nabla_\eta \pi - \int_0^\eta \nabla_\eta \cdot (m\mathbf{v}_h) d\eta, \\
\nabla_\eta(gw) &= \nabla_\eta(gw_s) + \int_\eta^1 \nabla_\eta \left(d\frac{mR_dT}{p} \right) d\eta, \\
w_s &= \mathbf{v}_{h,s} \cdot \nabla_\eta \Phi_s,
\end{aligned}
$$

(4)

where subscript $_s$ denotes surface values.

The total derivative operator on the left-hand sides of equations (3), $d/dt \equiv \partial/\partial t + \mathbf{v}_h \cdot \nabla_\eta + (d\eta/dt)\partial/\partial\eta$, is discretised in a two-time-level semi-Lagrangian fashion. The Coriolis term may be treated as part of the advected velocities or implicitly, where the Coriolis force is added to linear terms to be treated in the semi-implicit scheme (although such a formulation can be implemented only in the unstretched unrotated version of IFS/ARPEGE) (Temperton, 1997). For the NH-IFS the implicit treatment of the Coriolis force had to be suitably modified to fit the revised semi-implicit elimination process of the nonhydrostatic model (Yessad, 2008).

The semi-implicit time discretisation — initially proposed by Robert et al. (1972) for the hydrostatic equations — is derived by subtracting from the governing model equations a system of equations linearised around an isothermal, quiescent, hydrostatically balanced and horizontally homogeneous reference state. The linear part is treated implicitly, whereas the discretisation of the nonlinear residual is explicit (Bénard, 2004; Bénard et al., 2004, 2005). As described in Bénard et al. (2009) the semi-implicit (SI) time discretisation is augmented by an iterative-centred-implicit (ICI) procedure, where the prognostic variables used in the computation of the nonlinear explicit residual as well as in the semi-Lagrangian trajectory calculations are updated at every iteration. The resulting linear system of equations can be reduced by suitable elimination of variables to a single Helmholtz equation — which is solved in spectral space (at every iteration of the ICI scheme) — provided that the discretised vertical operators fulfil the constraint $COR = 0$ with

$$
COR = \frac{c_{vd}}{R_d^2 T_r} \gamma \tau - \frac{c_{vd}}{R_d c_{pd}} \gamma - \frac{c_{vd}}{R_d T_r} \tau + \frac{c_{vd}}{c_{pd}} \nu,
$$

(5)

where γ, τ, ν are generic notations for the semi-implicit linear operators defined in Ritchie et al. (1995); Yessad (2008), c_{vd}, c_{pd} denote the specific heat constants for dry air, and T_r is the reference temperature introduced to control the stability of the numerical procedure in the presence of vertically propagating gravity waves.

There are two options for the choice of the advected vertical prognostic variable: Either the vertical velocity w is advected (GWADV-NH) or the new variable $\mathcal{D}$ (Bénard et al., 2009). The former case is closer to the

natural choice of prognostic vertical variable. However, this choice requires an explicit conversion from w to $\mathscr{D}$, because the variable $\mathscr{D}$ is used in the linear part of the semi-implicit scheme.

If the ICI scheme is used, the total derivative of the residual $\mathscr{X}$ is also updated every time-step and implicitly contains all contributions from the physical parametrizations if these are included at the beginning of the time-step, cf. Wedi (1999) for a review. This is the $ND4SYS = 1$ option used in the ARPEGE, ALADIN and AROME setup (Bénard et al., 2009). However, in the NH-IFS only the adiabatic advective part of $d\mathscr{X}/dt$ is taken into account in all iterations of the ICI scheme, as the physics are currently called only once at the end of the last iteration. This lead to an instability which is remedied by recomputing $\mathscr{X}$ using provisional values at $t + \Delta t$ (including physics) and updating $\mathscr{D} = d + \mathscr{X}$ before the spectral computations (option $ND4SYS = 2$). Notably, option $ND4SYS = 2$ appears to be equally beneficial in removing some near surface noise over steep orography in adiabatic runs.

The horizontal discretisation of the NH model is spectral and identical to that of the hydrostatic IFS. The vertical discretisation is finite-difference (FD) as described in Bubnová et al. (1995) and Bénard et al. (2009).

In the operational version of the H-IFS a vertical finite-element (VFE) discretisation based on cubic B-splines is used (Untch and Hortal, 2004). An equivalent VFE scheme has not yet been successfully implemented in the NH model. The difficulties arise in the semi-implicit computations because the VFE discretised equivalents of the operators in (5) do not fulfil this constraint. However, an intermediate idea has been implemented and tested, where the FD discretisation is used in the linear (implicit) part and the VFE discretisation for the non-linear (explicit) part. The vertical integrals occurring in the non-linear part of the NH-IFS are similar to those in the H-IFS, and this part of the model remains very close to its hydrostatic counterpart, e.g. the calculation of Φ, $\nabla_\eta \Phi$, the pressure gradient terms, gw, $g\nabla_\eta w$, and the integral of the horizontal divergence resulting from the continuity equation (cf. equations (3)-(4)). Details of this "intermediate" VFE discretisation are given in the Appendix.

The above nonhydrostatic equations currently assume the shallow-atmosphere approximation. Work is in progress towards evaluating the deep-atmosphere formulation following Wood and Staniforth (2003) and its deep-hydrostatic counterpart (White and Bromley, 1995).

3 Performance assessment of the NH-IFS

In contrast to the filtered anelastic (e.g. EULAG) or hydrostatic equations (e.g. H-IFS), the fully compressible equations contain characteristic solutions with all three distinct wave propagation speeds: acoustic, gravity and advective. For validation purposes, a range of test cases aim to investigate the behaviour of the numerical implementation in NH-IFS for all these waves before assessing the overall model performance for global weather forecasts at hydrostatic and nonhydrostatic scales. The small-scale test cases adopt the testing framework described in Wedi and Smolarkiewicz (2009), where the size of the spherical computational domain is reduced by reducing the radius of the sphere without changing the depth or the vertical structure of the atmosphere. The shallow-atmosphere approximation is applied in all test cases shown and for NH-IFS (GWADV-NH) is used unless stated otherwise.

3.1 Spherical acoustic wave

This test is designed to validate the effectiveness of the semi-implicit algorithm in the nonhydrostatic model. The classical problem of a spherical acoustic wave is studied; cf. Landau and Lifschitz (2004), Problem 1 in section 70, chapter VIII. The problem considers "a sound wave in which the distribution of density, velocity

and other flow variables, depends only on the distance from some point". The analytic solution describes a spherical shell of thickness $2r$, where $r \in [c_o t - r_0, c_0 t + r_0]$, propagating away from the initial perturbation of radius r_0 with the acoustic propagation speed $c_0 = \sqrt{\gamma_0 R_d T_0}$, where R_d is the specific gas constant for dry air, $T_0 = 288.15$ K is the temperature of the assumed isothermal atmosphere and $\gamma_0 = 7/5$. An initial hemispheric pressure perturbation with $r_0 = a/6$ is set in an isothermal atmosphere at rest at the equator of a sphere with a radius one hundred times smaller than the radius of the Earth $a_E = 6371.229$ km ($a = a_E/100$). Within $r \leq r_0$ the constant initial (hydrostatic) pressure perturbation is prescribed as $\delta p/p_0 = 0.082$ where $p_0 = 1000$ hPa. The analytic solution for the pressure distribution within the propagating spherical shell is

$$p(r) = p_0 + \frac{(r - c_0 t)}{2r} (\gamma_0 \delta p).$$
(6)

The air is compressed in the outer portion of the shell $r > c_0 t$ and rarefied in the inner portion $r < c_0 t$; cf. Smolarkiewicz and Szmelter (2008). For prescribing the initial condition in the model and for plotting purposes, the vertical and horizontal distances are computed separately, with the horizontal distance r_h measured along a great circle on the sphere with $r_h(\lambda, \phi) = a \cos^{-1}[\sin \phi \sin \phi_c + \cos \phi \cos \phi_c \cos(\lambda - \lambda_c)]$ from the reference point centred at $(\lambda_c, \phi_c) = (3\pi/2, 0)$. The vertical distance for $r_h < r_0$ is computed from $r_v = r_h \tan(\cos^{-1}(r_h/r_0))$.
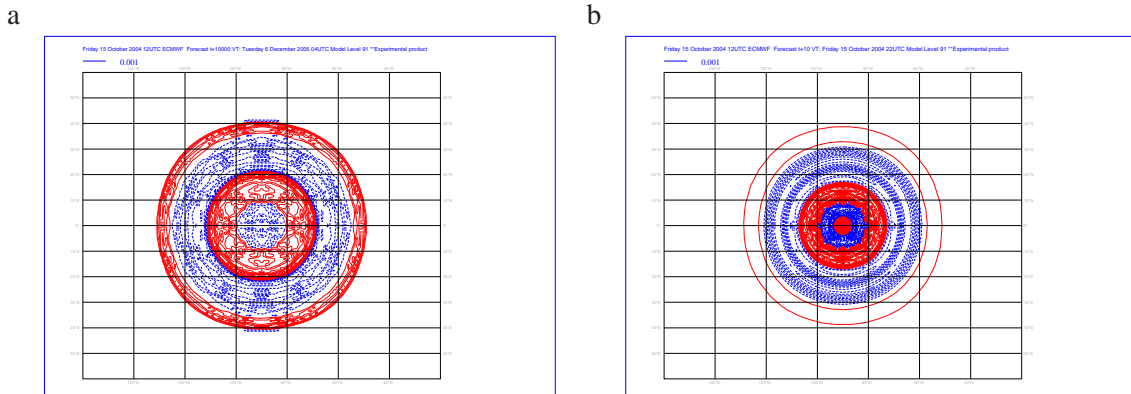

Figure 1: Spherical sound wave from the explicit simulation with timestep $\Delta t = 0.01$ s (panel a) and from the semi-implicit simulation with $T_r = 350$ K, $T_{ra} = 100$ K and timestep $\Delta t = 10$ s (panel b). The figure shows normalised pressure perturbation $\delta p/p_0$ at the lowest model level after 100 s.

Figure 1 illustrates the horizontal propagation of the pressure perturbation for the explicit simulation, requiring for numerical stability the prohibitively short time-step $\Delta t = 0.01$ s, and the semi-implicit simulation with $\Delta t = 10$ s. The propagation speed of the acoustic wave in the horizontal direction is not modified by the semi-implicit integration with 1000 times the explicit timestep but the amplitude is distorted. Both simulations give the correct spherical shell with thickness $2r_0$ and a propagation speed $c_0 \approx 340$ ms^{-1} reflecting the theoretical value of the acoustic speed given above.

The stability of the semi-implicit NH-IFS model is controlled by the setting of a reference temperature for the propagation of gravity waves T_r and another reference temperature T_{ra} controlling the propagation of acoustic waves. The over-implicitness of the semi-implicit scheme is given by the ratio T_r/T_{ra}. Also in this acoustic wave case (in a stably stratified atmosphere) it is verified that the numerical model is only stable for $T_r > T_0$ (Temperton and Simmons, 1997).

A series of tests show that the choice of T_{ra} is restricted for this case to 10 K$< T_{ra} < T_r$. Panel b in Fig. 1 has been obtained with $T_{ra} = 100$ K and $T_r = 350$ K and 5 iterations of the ICI scheme ($N_{iter} = 5$). Figure 2 illustrates the propagation of the sound wave in the vertical direction. Panel a shows the explicit solution and
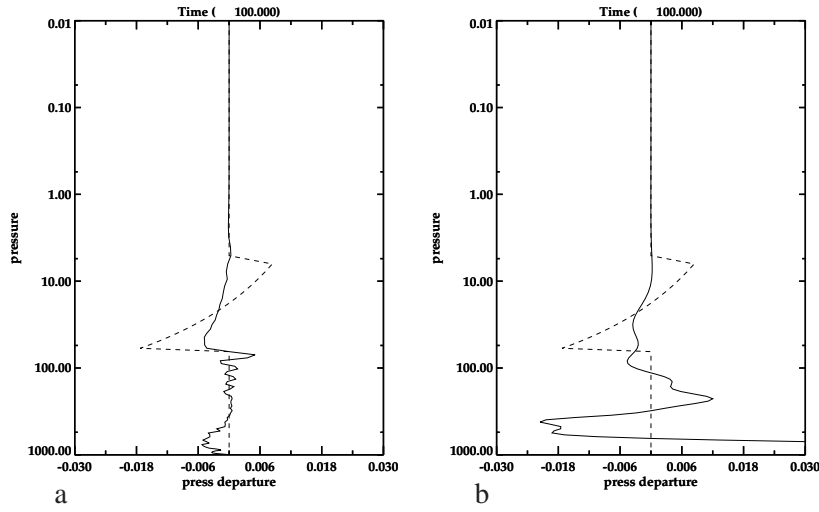
Figure 2: Spherical sound wave: comparison of the pressure perturbation after 100 *s in the vertical direction with the analytic solution (dashed) for a) the explicit NH-IFS simulation (solid) with timestep $\Delta t = 0.01$ s and b) the semi-implicit NH-IFS simulation (solid) with timestep $\Delta t = 10$ s.*

panel b the semi-implicit solution after 100 s. The amplitude is reduced in the explicit simulation compared to the analytic solution. The propagation speed, however, remains approximately 340 ms^{-1}. In contrast, the semi-implicit simulation with $\Delta t = 10$ s gives a distorted amplitude and the sound wave is artificially slowed down in the vertical direction as expected. The near surface perturbation seen in panel b of Fig. 2 oscillates in amplitude with time. Notably, the semi-implicit case with timestep $\Delta t = 1$ s and the explicit case are nearly identical, with the semi-implicit even better representing the analytic solution (not shown). The number of iterations of the ICI scheme do not affect the qualitative nature of the result but they affect the amplitude of the perturbation and its oscillation in time. This behaviour may be of some concern, when acoustic perturbations are excited near the surface in real weather applications, although the amplitude is likely to be much smaller compared to the much exaggerated initial pressure perturbation discussed here.

3.2   Bubble experiments

This example illustrates the failure of the hydrostatic model version at nonhydrostatic scales for the evolution of a large cold bubble with a tiny warm bubble added to break the symmetry (Robert, 1993) — prescribed as potential temperature perturbations in a neutrally stratified environment $\theta \equiv T(p/p_0)^{-R/c_p} = \theta_0 = const.$ with $p_0 = 1000$ hPa and $\theta_0 = 300$ K. Notably, the results presented here are three-dimensional simulations in contrast to the original proposal in Robert (1993). The IFS is run on the reduced-size planet with radius $a = 30km$ in a standard T_L159 resolution with an equivalent linear reduced Gaussian grid (320 points along the equator) with the operational 91 vertical level distribution. Potential temperature perturbations of the bubbles are of the form

$$\theta(r_i) = \begin{cases} \theta_i' & \text{if } r_i \leq 1, \\ \theta_i' e^{-r_i^2/s^2} & \text{otherwise,} \end{cases} \qquad (7)$$

where $s = 1/3$ and $r_i = \sqrt{(l_i/L_{l_i})^2 + ((h - h_i)/L_{h_i})^2}$ with $h = -R_d\theta_0/g \log(p/p_0)$ and $l_i = a\cos^{-1}[\sin\phi \sin\phi_c + \cos\phi \cos\phi_c \cos(\lambda - \lambda_{c_i})]$. The cold bubble ($i = 1$) has a perturbation amplitude $\theta_1' = -0.5$ K with its centre located at $(\lambda_{c_1}, \phi_c) = (3\pi/2, 0)$ and height $h_i = 15$ km. The horizontal width and height of the cold bubble are $L_{l_1} = 10$ km and $L_{h_1} = 4$ km, respectively. The warm bubble ($i = 2$) has perturbation amplitude $\theta_2' = +0.15$ K with dimensions $L_{l_2} = 0.6$ km and $L_{h_2} = 0.6$ km, with its centre location offset by six gridpoints in longitudinal direction at height $h_2 = 6$ km. There is no analytic solution for this case. The results are compared with the
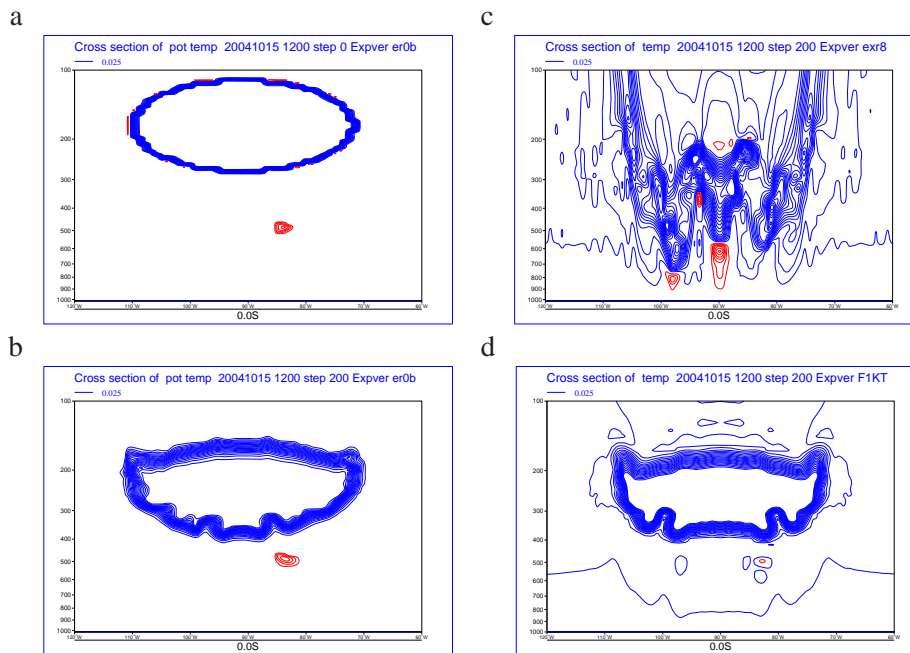
Figure 3: Potential temperature distribution in an equatorial cross section at t=0 (Panel a) and after t=1000s (Panel b-d) for a run with an initial large cold bubble and a small warm bubble as depicted in panel a. Panel b is from the EULAG simulation while panel c and d are from the hydrostatic and the NH-IFS model simulations, respectively. Contour interval is 0.025 *K.*

solutions of EULAG, which utilises a latitude-longitude grid of $320 \times 144 \times 421$ with $dz = 300$ m. The timestep is 5 s, and both models use a semi-Lagrangian scheme. EULAG makes the Boussinesq approximation in this case.

Panel a in Fig. 3 shows the initial state for this problem. Panel b shows the result from the EULAG simulation while panel c and d show the solution with the hydrostatic and the NH-IFS, respectively after 1000s of simulation. The IFS and EULAG results are similar at this point but IFS is more diffusive. The test case clearly discriminates between the hydrostatic and the nonhydrostatic solution, as can be seen by comparing panel c and d of Fig. 3. Figure 4 depicts the time instants at $t = 1800$ s and $t = 2400$ s for both the IFS and EULAG. A faster downward propagation is noted in the case of EULAG and the bubble shapes differ at the later time. Once the bubble interacts with the lower boundary, further differences are noted in the subsequent roll-up motion with faster propagation again in the case of EULAG (not shown). The overall evolution is indicative of the correct nonhydrostatic behaviour. The bubble shape is sensitive to the details of the numerical scheme such as the amount of explicit or implicit diffusion and the truncation error, as has been noted by other authors, cf. Robert (1993); Grabowski and Smolarkiewicz (1990).

3.3 Orographically-forced flow in the limit of marginally resolved topographic features

The flow past a given terrain profile under stably stratified atmospheric conditions is a canonical problem in meteorological studies, since it illustrates the far-field effect via long-range transport of waves, affecting large parts of the computational domain.

Simulations of orographically-forced atmospheric gravity waves have been conducted with NH-IFS for a range of orographic profiles: bell-shaped, Gaussian, quasi-2D elliptic, a Himalaya-like step-mountain, and the mountain profile proposed in Schär et al. (2002). The latter two stress the numerical implementation in the limit of
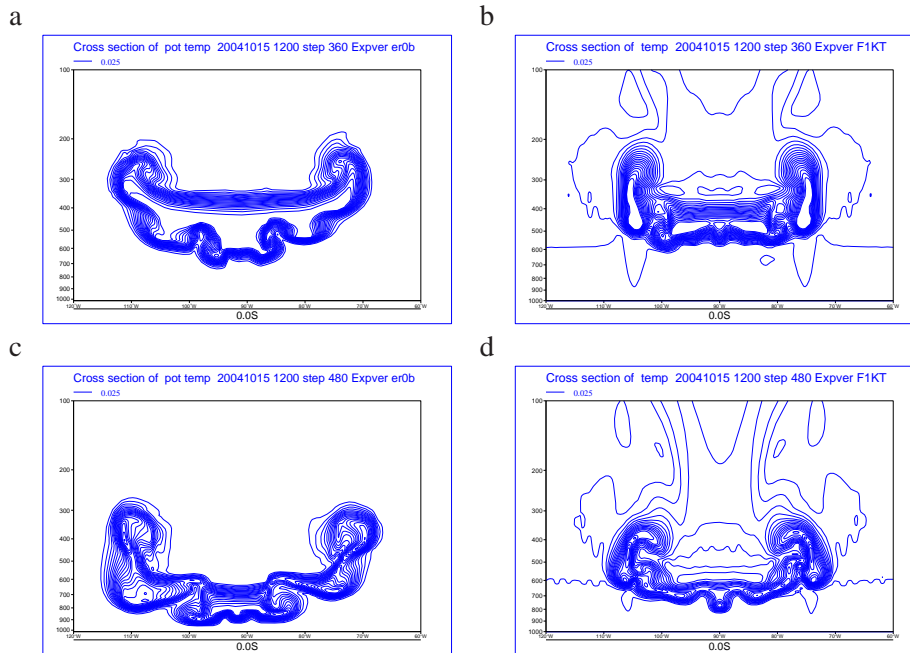
Figure 4: Potential temperature distribution at $t = 1800\ s$ (Panel a and b) and $t = 2400\ s$ (Panel c-d) for EULAG (panel a and c) and the NH-IFS (panel b and d). Contour interval is $0.025\ K$.

marginally resolved orographic features. The selected parameters of the problem favour bifurcation into a qualitatively incorrect solution; cf. (Klemp et al., 2003) for a discussion. The specific terrain profile (Schär et al., 2002) is given as

$$h(\lambda, \phi) = h_0 e^{-l^2/L_\lambda^2} \cos^2\left(\frac{\pi l}{\zeta}\right), \tag{8}$$

with $l(\lambda, \phi) = a \cos^{-1}[\sin\phi \sin\phi_c + \cos\phi \cos\phi_c \cos(\lambda - \lambda_c)]$ centred at $(\lambda_c, \phi_c) = (3\pi/2, \pi/6)$; $h_0 = 0.25$ km, $L_\lambda = 5$ km and $\zeta = 4$ km, defining the deviation from a bell-shaped hill. Ambient conditions consist of the uniform wind profile $u_e(z) = U = 20$ ms^{-1}, $(v_e = 0, w_e = 0)$ and a Brunt-Väisälä frequency $N = 0.018$ s^{-1}. The vertical spacing used in the IFS simulation is equivalent to the operational 91 level configuration with $\Delta z \leq 600$ m until approximately 200 hPa. The IFS is run with a reduced-size sphere of radius $a = 30$ km in a standard $T_L 159$ resolution with an equivalent linear reduced Gaussian grid (320 points along the equator), which is approximately equivalent to $\Delta x = \Delta y = 589$ m. The time-step is 10 s.

The correct solution is a weak-amplitude mountain wave above the main topography profile. In the three dimensional adaptation presented here, there is in addition a large-amplitude nonhydrostatic response in the lee of the mountain, which is not found in the 2D simulations (Klemp et al., 2003). The EULAG model result (not shown) has the same 3D behaviour as in IFS for this test case, while being equivalent to the 2D result in a corresponding 2D simulation (Wedi and Smolarkiewicz, 2004), suggesting that this is a feature of the 3D setup. This test is particularly useful in exposing problems with the discretisation near the lower boundary as shown in Fig. 5. Vertical "chimneys" in vertical velocity are excited at the low points of the wavy mountain profile and extend vertically throughout the whole atmosphere. These have also been found in limited-area simulations with the NH-ALADIN model (Geleyn, 2005). Notably, the hydrostatic model H-IFS does not show this problem but a qualitatively different solution with larger amplitude (panel b in Fig.5, contour interval four times larger). Two solutions have been proposed as summarised in Geleyn (2005). In the preferred option GWADV-NH (panel d in Fig. 5) the specification of the lower boundary of w is straight forward, since the vertical velocity is on half-(model) levels, thus coincides with the lower boundary. Otherwise, it is necessary to
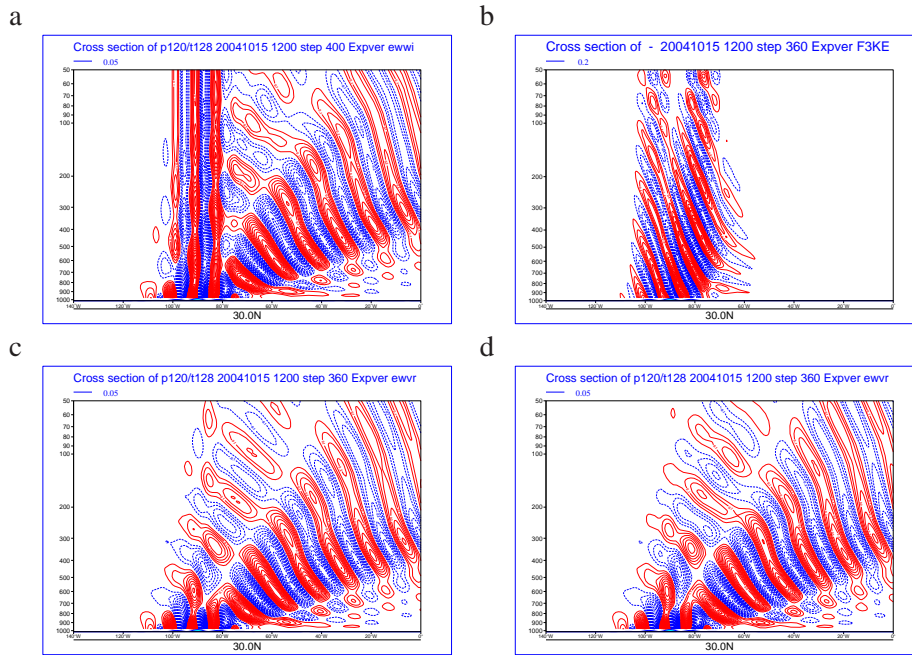
Figure 5: Vertical velocity for the flow past the terrain profile given in (8) after 1 hour of simulation. Panel a shows the development of vertical "chimneys" in the control NH-IFS simulation. Panel b is the result with the hydrostatic model H-IFS. Panel c is the NH-IFS result with LRDBBC = T and panel d is the NH-IFS result for GWADV-NH. The contour interval in panels a,c-d is the same as in Klemp et al. (2003), 0.05 ms^{-1}. Panel b has contour interval 0.2 ms^{-1}.

suitably modify the lower boundary condition consistent with the semi-Lagrangian advection scheme (Geleyn, 2005; Bénard et al., 2009), that is to calculate dw_s/dt in a semi-Lagrangian fashion (option $LRDBBC = T$) (panel c in Fig.5), rather than constructing the total derivative from the expression for w_s in the last equation of (4).

3.4 Quasi two-dimensional orographic flow with linear vertical shear

This classical problem — studied in, e.g., Wurtele et al. (1987); Keller (1994) — constitutes a particularly discriminating test, because in the presence of shear the nonhydrostatic and hydrostatic equations predict a fundamentally different propagation of orographically-forced gravity waves. While hydrostatic models produce a vertically propagating mountain gravity wave, the correct solution is that of a trapped, horizontally propagating gravity wave. For a direct comparison with the published analytical results the same parameter space as in Keller (1994) is explored but with a suitably modified mountain to accommodate the global spherical geometry of the models.

The mountain is a three-dimensional elliptic adaptation of the classical "witch of Agnesi" profile centred at the equator

$$h(\phi, \lambda) = h_0 \left(\left(1 + (l_\lambda/L_\lambda)^2\right) + \left(l_\phi/L_\phi\right)^2 \right)^{-1} \tag{9}$$

with $l_\lambda = a \cos^{-1}[\sin^2 \phi_c + \cos^2 \phi_c \cos(\lambda - \lambda_c)]$ and $l_\phi = a \cos^{-1}[\sin \phi_c \sin \phi + \cos \phi_c \cos \phi]$, where the mountain half-width is $L_\lambda = 2.5$ km, and the meridional extent of the ellipse is defined by $L_\phi = |L_\lambda^2 - L_f^2|^{1/2}$, the centre position of the mountain $(\lambda_c, \phi_c) = (3\pi/2, 0)$, and the focus point distance $L_f = a \cos^{-1}[\sin \phi_d \sin \phi_c + \cos \phi_d \cos \phi_c \cos(\lambda_d - \lambda_c)]$ with $(\lambda_d, \phi_d) = (3\pi/2, \pi/3)$; mountain height is $h_0 = 100$ m. All distances and formulae are expressed following great circles on the sphere. Ambient conditions consist of the linearly

sheared wind profile $u_e(\phi, z) = U_0(1 + cz) \cos(\phi)$ below the tropopause located at 10.5 km, and constant aloft; $U_0 = 10$ ms^{-1} and $c = 2.5 \times 10^{-4}$ m^{-1}; ($v_e = 0, w_e = 0$) and the Brunt-Väisälä frequency $N = 0.01$ s^{-1}. The Richardson number of the flow in the troposphere is $Ri \equiv N^2/(U_0 c)^2 = 16$ and in the stratosphere $Ri = \infty$. To facilitate comparison with the IFS — formulated in temperature rather than potential temperature — the models are set in isothermal ambient conditions without the stability jump employed in Wurtele et al. (1987). This simplifies the specification of a constant stability, since with potential temperature $\theta = T(p/p_0)^{-R/c_p}$ and the hydrostatic relation $\partial \ln p/\partial z = -g/RT$ the atmospheric stability may be expressed as

$$S = \frac{\partial \ln \theta}{\partial z} = \frac{\partial \ln T}{\partial z} - \frac{R}{c_p} \frac{\partial \ln p}{\partial z} = \frac{\partial \ln T}{\partial z} + \frac{g}{c_p T}. \tag{10}$$

Thus, an atmosphere with constant stability $S = N^2/g$ is equivalent to an isothermal atmosphere with $T_0 = g^2/(c_p N^2)$. In both models, the same sheared, isothermal, zonal flow on the sphere is analytically prescribed at initial time and is maintained in the absence of other forcings.
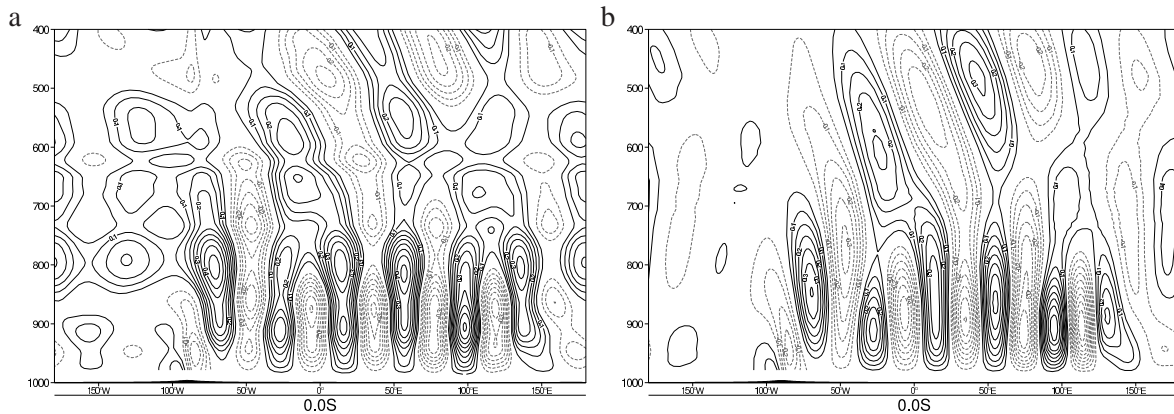

Figure 6: *Vertical cross-section at the equator of vertical velocity after two hours of simulation, comparing the NH-IFS (Panel a) with EULAG (Panel b) for a linearly-sheared flow past a quasi-two-dimensional "witch of Agnesi" obstacle on the sphere. The wind velocity is constant above 10.5 km (or ≈ 687 hPa). Contour interval is 0.05 ms^{-1}. Solid/Dashed lines denote positive/negative contours. The vertical axis is pressure in hPa.*
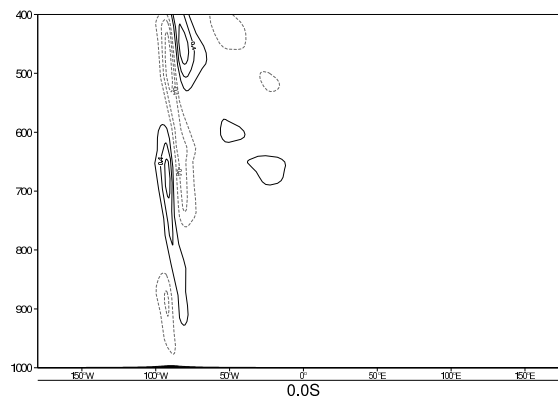

Figure 7: *Same as in Fig. 6 for the hydrostatic version of the IFS after two hours of simulation. The solution is consistent with the hydrostatic analytic solution (Keller, 1994, Fig. 2). In contrast to Fig. 6 the wave propagation is entirely vertical. Contour interval is 0.2 ms^{-1}.*

The EULAG domain size is $512 \times 228 \times 121$ with a horizontal and vertical grid spacing of 250 m, which corresponds to a radius of the sphere $a = 20.3718$ km. The IFS is run with a $T_L 255$ resolution with an equivalent linear reduced Gaussian grid (512 points along the equator) with 115 vertical levels. The lowest 15 km have

the same vertical spacing of 250 m as in EULAG. The integration time is 2 h with a time step $\Delta t = 5$ s for both models. For the hydrostatic IFS, the solution is characterised by an entirely vertical response to the mountain forcing; cf. Keller (1994). Here vertical absorbers are important to avoid reflection at the model top and to obtain the analytic solution for an unbounded atmosphere. Therefore, the damping profile $\alpha = \tau^{-1} \sin^2(Z - Z_{thres})/(Z_{top} - Z_{thres})\}$ (Klemp and Lilly, 1978) has been applied in the hydrostatic IFS above $Z = Z_{thres} = 350$ hPa with attenuation time scale $\tau = 50$ s. The upper limit of the IFS is formally always at $p = 0$, whereas a rigid lid upper boundary at 25 km was chosen in EULAG for computational efficiency. While in the NH-IFS no absorbers are used, in EULAG the damping profile $\alpha = \tau^{-1} \max\{0, (Z - Z_{thres})/(Z_{top} - Z_{thres})\}$ is applied with $Z_{thres} = 20$ km and $\tau = 300$ s.
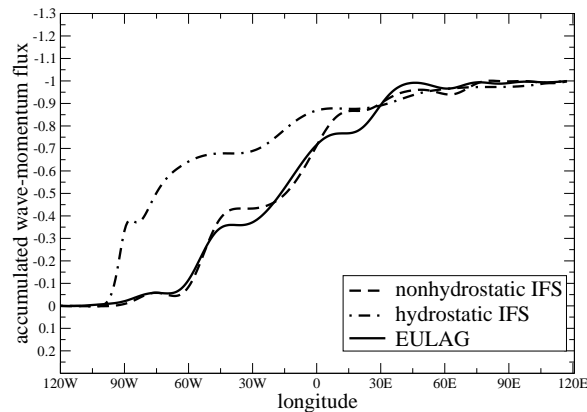

Figure 8: Running sum of $\rho_0(u - [u])(w - [w])$ at 700 hPa, meridionally averaged over ± 10 degrees latitude. The dashed line is for the NH-IFS (Fig. 6 a), the solid thick line denotes EULAG (Fig. 6 b) and the dot-dashed line shows the hydrostatic IFS solution. The mountain is centred at $90°$ W. Values are relative to the final integrated value.

Panel a in Fig. 6 shows the vertical velocity after two hours simulated with the NH-IFS, and panel b shows the reference solution with EULAG. The nonhydrostatic solutions may be compared with the solution obtained with the hydrostatic IFS (Fig. 7), which is consistent with the analytic solution (maximum contours 0.6ms^{-1}) of the same case presented in Keller (1994). The hydrostatic model fails to represent the trapping and the horizontal propagation of lee waves. The nonhydrostatic solutions in Fig. 6 compare quantitatively well. Specifically, there are closed cells behind the mountain with an approximate horizontal wavelength of 14 km in agreement with the linear analysis and with the numerical solution of a similar case in Wurtele et al. (1987). The numerical solution (cf. Wurtele et al., 1987, Fig.11) was obtained with a stability jump between troposphere and stratosphere and a mountain height of 500 m. However, as the amplitude of the analytic solution scales with the mountain height, the amplitudes in Fig. 6 may simply be multiplied by a factor five, which gives amplitudes in EULAG of $1.75 - 1$ms^{-1} and in IFS $2.25 - 1$ms^{-1}, compared to $1.6 - 0.8$ms^{-1} in Wurtele et al. (1987). Given, that the same horizontal wavelength (14 km) is obtained in Fig.6, it suggests that the stability jump mostly influences the leakage of wave energy above the tropopause, located at 10.5 km. Thus in comparison to Wurtele et al. (1987), a different decay of amplitude with distance from the mountain is expected, but not the qualitative nature of the lee wave solution. Interestingly, both models show the same albeit weak second mode — indicated by the increase in amplitude of some of the cells — which is not expected according to the linear analytic theory and the numerical solution in Wurtele et al. (1987). In agreement with the dispersion relation, after two hours the stratospheric gravity waves already arrive upstream of the mountain. The gravity waves leaked into the stratosphere are reflected at the model top and the downward and horizontally propagating waves are modulated by the shear transition imposed at 10.5 km, which leads ultimately to differences between the

two solutions in Fig. 6, with IFS being noisier. The time evolution of the flow (not shown) indicates that the differences arise due to the different upper boundary condition. The damping profile applied in the hydrostatic simulation proved ineffective for the NH-IFS. Experiments showed that the effectiveness and the applicability of "sponge" layers at the IFS model top, such as recently proposed in Klemp et al. (2008), were limited due to the (vertical) derivative prognostic variable and the type of vertical coordinate.
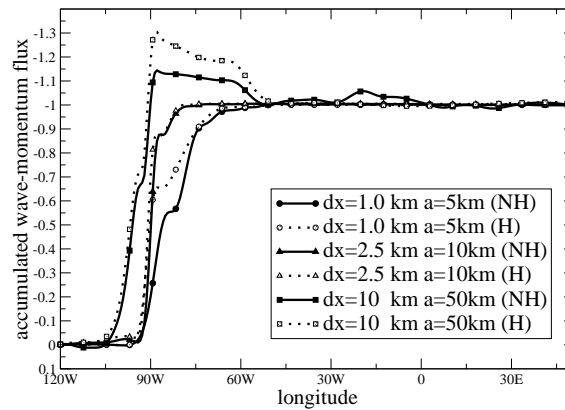

Figure 9: Running sum of $\rho_0(u - [u])(w - [w])$ at 700 hPa, meridionally averaged between ± 10 degrees latitude, for hydrostatic (H, dotted lines) and NH-IFS (NH, solid lines) simulations with gridsizes $dx = 10$ km (squares), $dx = 2.5$ km (triangles) and $dx = 1$ km (circles), respectively. The mountain is centred at $90°$ W. Values are relative to the final integrated value. Because the angular grid increment is fixed, the linear distance for each graph is different.

The nonhydrostatic wave is associated with a characteristic downstream shift of the vertical flux of horizontal momentum, which represents an additional measure for quantifying the difference between hydrostatic and nonhydrostatic solutions; cf. the corresponding Figs. 11 and 12 in Keller (1994). In Fig. 8 the running sum of the wave-momentum flux along the equator is compared for the cases depicted in Fig. 6 and Fig. 7, respectively. The accumulated wave-momentum flux is evaluated at a constant pressure surface as

$$\mathscr{S}_{i_k} = \left\langle \sum_{i=i_s}^{i_k} \rho_0(u(\lambda_i, \phi) - [u])(w(\lambda_i, \phi) - [w]) \right\rangle, \qquad (11)$$

where $[\ ]$ denotes the zonal average and $\rho_0 = p/RT_0$; the $\langle\ \rangle$ symbolises an average over ± 10 degrees latitude. The zonal index i_s of the running sum corresponds to 30 degrees west of the centre of the mountain, and $i_k = i_s, .., i_n$ with index i_n corresponding to 210 degrees east of the mountain, cf. section 4d in Keller (1994) for a discussion. The results in Fig. 8 are qualitatively similar to the analytic results in Keller (1994) and both the NH-IFS and EULAG simulations show the characteristic downstream shift of the nonhydrostatic solution.

In addition, a series of cases with half the ratio L_λ/dx used above (i.e. $L_\lambda/dx \equiv 5$) for $dx = 10., 5., 2.5, 1., 0.25$ km, and the correspondingly reduced radii of the computational sphere, were run to illustrate the transition between the hydrostatic and the nonhydrostatic regime in NWP models with marginally resolved orography. Figure 9 quantifies the convergence towards hydrostatic model behaviour with increasing grid-size. The characteristic solution disparity between the nonhydrostatic and the hydrostatic IFS appears below $dx = 2.5$ km, but only at $dx = 1$ km the results are significantly different in the lee of the mountain. For $dx = 1$ km and $dx = 0.25$ km (Fig. 8) the difference of the solutions in the lee of the mountain persists over some distance, while at $dx = 10$ km both solutions show the characteristic hydrostatic behaviour. However, the hydrostatic IFS produces a larger amplitude of the wave momentum flux right above the mountain top. In general, the

transitional resolution between hydrostatic and nonhydrostatic regimes depends on the ratio of the characteristic horizontal and vertical scales involved. Although the simulations represent only a narrow region in a large parameter space, the results are consistent with estimates typically obtained from a heuristic scale analysis of nonhydrostatic motions in NWP, i.e. horizontal scales $L = \mathcal{O}(10\,\text{km})$ resolved with grid intervals $dx = \mathcal{O}(2\,\text{km})$.

3.5 The critical level effect on linear and non-linear flow past a three-dimensional hill

The transfer of energy and momentum from smaller scale fluctuations toward an emerging mean flow represents a fundamental mechanism influencing the predictability of weather and climate. The numerical realisability of propagating waves at internal critical layers is equally important for mesoscale orographic flows (Grubišić and Smolarkiewicz, 1997) as for the planetary circulation, e.g. the quasi-biennial oscillation (Wedi and Smolarkiewicz, 2006). The critical level is a preferred location for internal wave breaking, with the resulting flow locally nonlinear and nonhydrostatic. Yet, when mean wind curvature vanishes everywhere and the mean wind velocity decreases with height, the hydrostatic approximation can be justified — given horizontal wavenumbers $k \ll N/U(z=0) < \infty$ — thus facilitating the development of linear solutions. The effect of a critical level on the airflow past an isolated axially symmetric hill has been studied in Grubišić and Smolarkiewicz (1997). In their work nonhydrostatic effects were minimised to verify the linear theory with a nonlinear nonhydrostatic model. This test case thus represents a nonhydrostatic benchmark with an analytic solution in the hydrostatic limit. It is used here to test the asymptotic behaviour of NH-IFS.
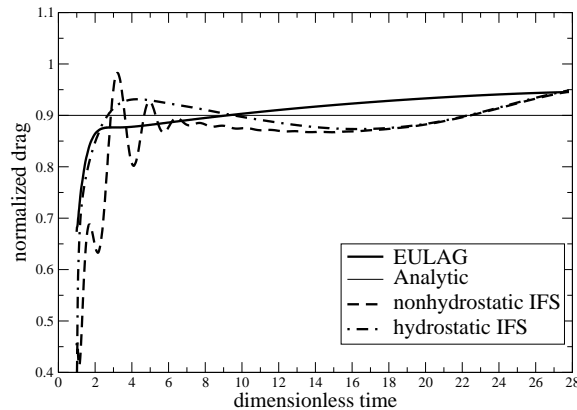

Figure 10: *Comparison of the zonal drag history for NH-IFS, hydrostatic IFS, and EULAG for the linear critical flow past a three-dimensional hill on the sphere (LS2). The drag is normalised by $D_0 = \pi/4\rho_0 NU_0 ah_0^2$ (Grubišić and Smolarkiewicz, 1997). Time is nondimensionalised by $t^* \equiv tU_0/L_\lambda$. The analytic solution is denoted by the thin solid line. The dashed line is for the NH-IFS, the solid thick line denotes EULAG and the dot-dashed line shows the hydrostatic IFS solution.*

Two examples from Grubišić and Smolarkiewicz (1997), LS2 for a linear and LS5 for a non-linear flow, are adapted to the sphere. The bell-shaped mountain is represented by

$$h(\lambda, \phi) = h_0 \left(1 + l(\lambda, \phi)^2/L_\lambda^2\right)^{-3/2} \tag{12}$$

with $l(\lambda, \phi) = a\cos^{-1}[\sin\phi\sin\phi_c + \cos\phi\cos\phi_c\cos(\lambda - \lambda_c)]$ with $(\lambda_c, \phi_c) = (3\pi/2, 0)$. To facilitate a comparison with the results in Grubišić and Smolarkiewicz (1997), their setup is followed closely by specifying $U_0/NL_\lambda = 0.2$ in all experiments, with $U_0 = 10\,\text{ms}^{-1}$, $N = 0.01\,\text{s}^{-1}$, and $L_\lambda = 5000\,\text{m}$. The ambient wind

profile with a reverse linear shear is prescribed as $u_e(\phi, z) = U_0(1 - z/z_c)\cos(\phi)$, where $z_c = (U_0/N)\sqrt{Ri}$ is the height of the critical level for the stationary mountain wave. Both linear and nonlinear flow simulations are characterised by $Ri = 1$ and dimensionless mountain height $\hat{h} = h_0 N/U_0$. In the linear case $\hat{h} = 0.05$ (LS2), whereas in the non-linear case $\hat{h} = 0.3$ (LS5). As in previous test cases isothermal conditions are assumed to facilitate an equivalent setup in the IFS.
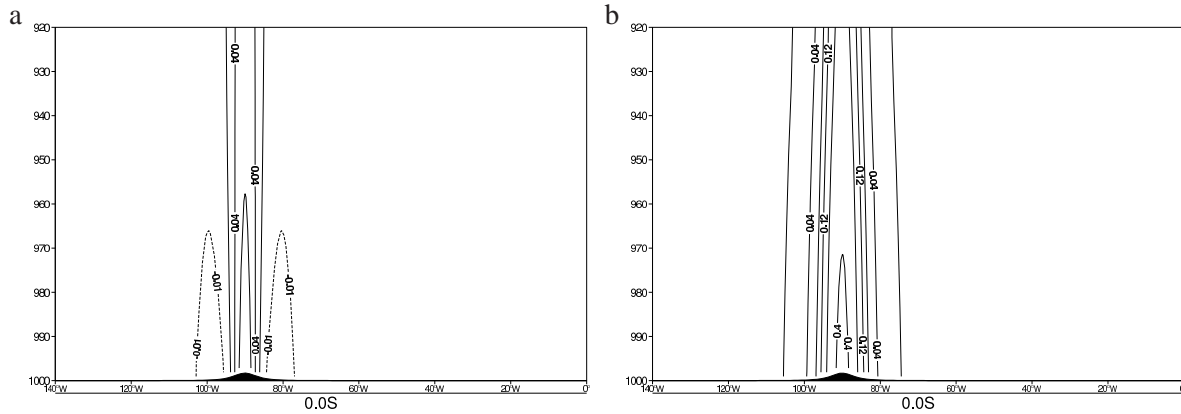

Figure 11: Zonal velocity perturbation from the LS2 run at initial time ($t^* = 0$) for (a) EULAG and (b) for the NH-IFS. Contours are from $-0.01\ ms^{-1}$ to $0.4\ ms^{-1}$.

The radius of the sphere is set as $a = 63.662$ km. EULAG utilises a latitude-longitude grid of $320 \times 144 \times 91$ with $dz = 35$ m. The IFS is run at $T_L 159$ resolution with an equivalent linear reduced Gaussian grid (320 points along the equator) with 120 vertical levels with constant spacing $dz = 35$ m in the lowest 2 km. The integration time is 6 h with a time step $\Delta t = 10$ s for both models. A simple sponge layer with the inverse of the attenuation time scale $\alpha = \tau^{-1}\max\{0, (Z - Z_{thres})/(Z_{top} - Z_{thres})\}$ has been added to both models. Particularly for the IFS this filters out some high frequency noise. For EULAG $Z_{thres} = 2.5$ km was chosen with $\tau = 300$ s. In the IFS the sponge was applied in pressure p with $Z = -p$, $Z_{thres} = -930$ hPa, $Z_{top} = 0$, and $\tau = 1000$ s.

To quantify the overall performance of NH-IFS, the drag — the total force exerted on the mountain by the flow — is measured as

$$\int_{-\infty}^{+\infty} \int_{-\infty}^{+\infty} p(x, y, z = h)\nabla h\ dxdy. \tag{13}$$

Figure 10 compares the zonal drag history in the linear LS2 case for the three different models, EULAG, the hydrostatic IFS and the NH-IFS. The analytic linear solution (Grubišić and Smolarkiewicz, 1997) is indicated by the thin solid black line. Initially, the NH-IFS differs strongly from EULAG, showing an oscillation of the zonal drag around the analytic solution. This can be explained by the different initialisation procedure between both models. While the identical analytic initial state is prescribed, in EULAG the "suitability" of the initial conditions is ensured by imposing a potential-flow perturbation on the prescribed ambient flow. This ensures that the initial conditions form a solution to the governing numerical problem; see Temam (2006) for a discussion. In contrast, the IFS was started from the analytic initial conditions without initialisation; thus, the mountain forces the system impulsively. In NWP the initialisation problem is well-known (cf. Daley, 1991, chap. 6), and in real weather applications the "suitability" of the initial condition for IFS is ensured through the process of variational data assimilation. For completeness, the initialised and the uninitialised zonal flow perturbation at $t^* = 0$ is illustrated in Fig. 11 for the LS2 case.

The resulting oscillations decay in time, and all numerical results approach the analytic steady-state. The zonal drag evolution in Fig. 10 is a running average over 100 points to filter out high frequency noise, initially present in the IFS solutions but decaying in time due to the vertical absorber applied. In the linear case, after an integration time $t^* \equiv tU_0/L_\lambda = 14$ (dimensionless) all models reach a near equilibrium state and the
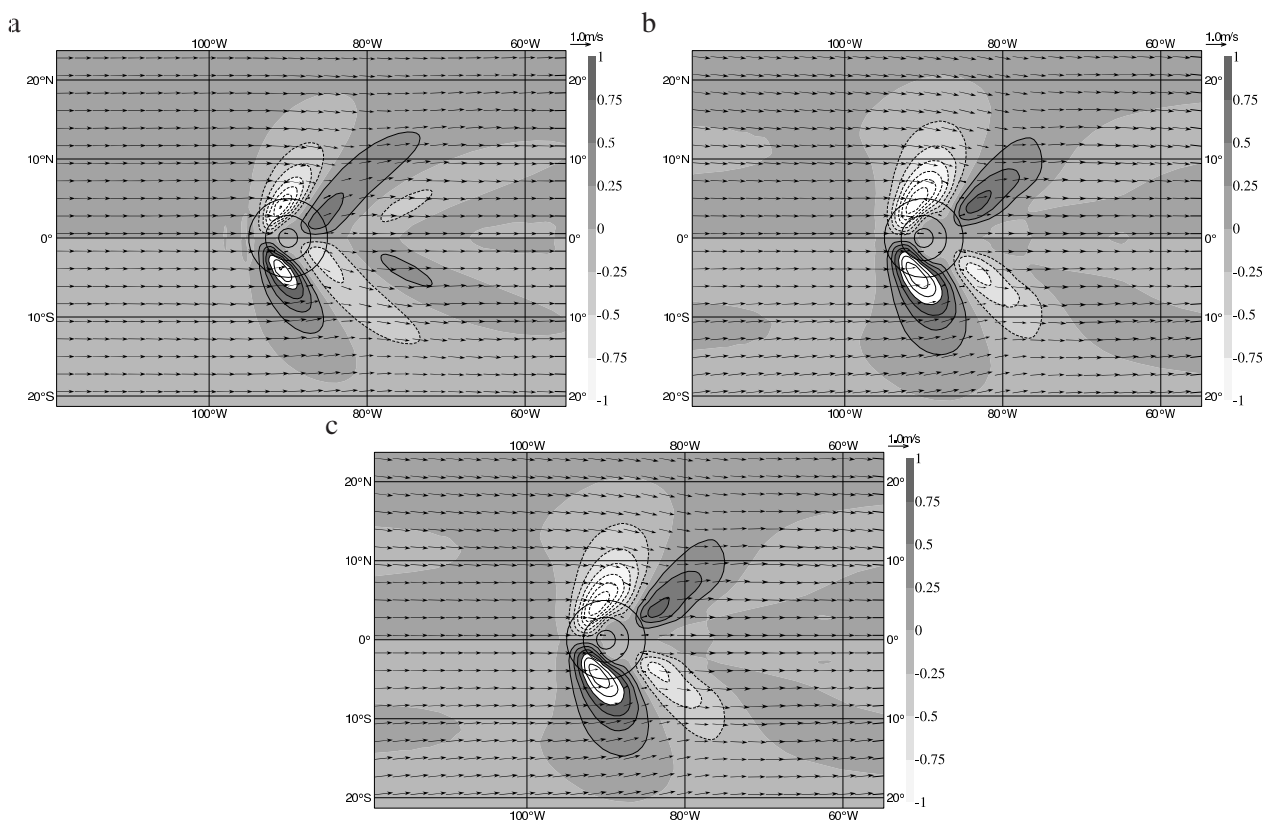
Figure 12: Vertical vorticity ($\times 10^{-4}$ s^{-1}) and corresponding velocity vectors from the LS2 run at $t^* = 28.8$. Panel a shows the EULAG solution in the horizontal plane at $z = 0.94z_c$. Panels b and c show the corresponding solutions for hydrostatic IFS and NH-IFS, respectively; panels b-c show the nearest IFS model level equivalent to $0.94z_c$ shifted by $3dz$ (see text for an explanation).
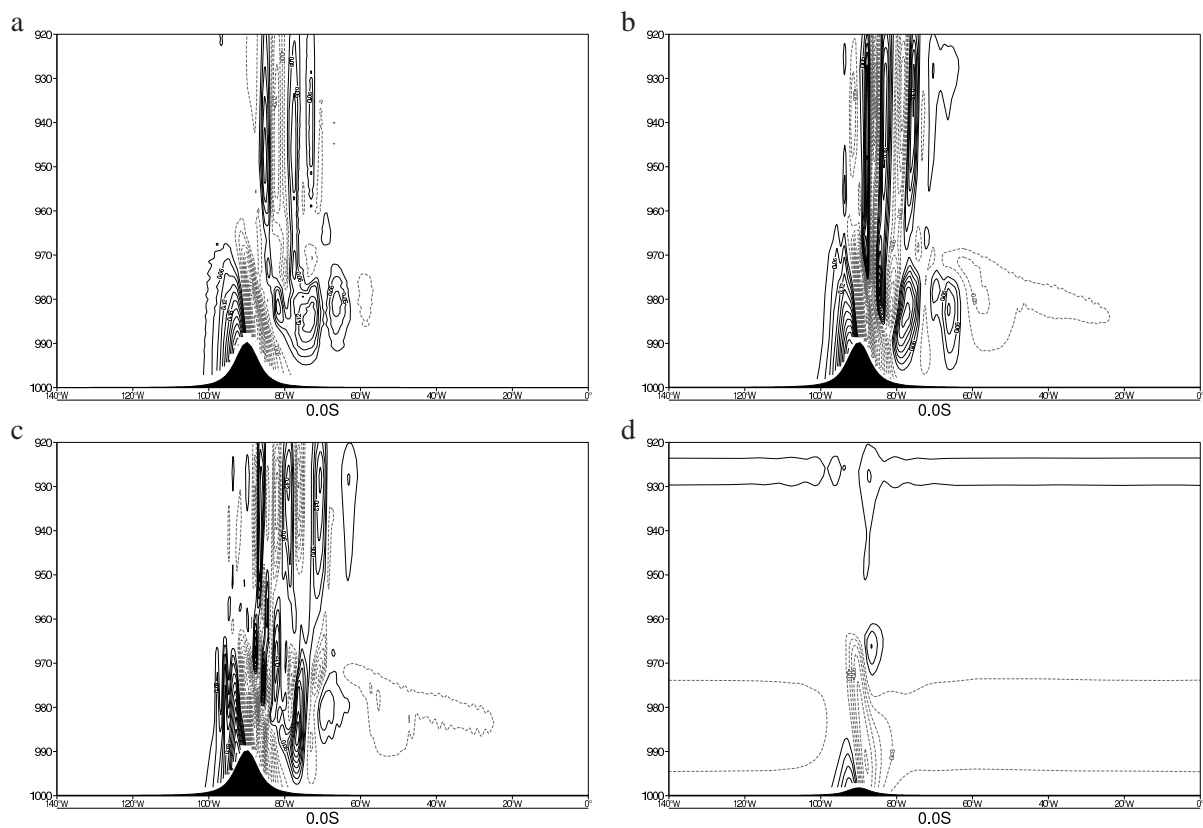
Figure 13: Vertical velocity from the LS5 run at $t^* = 43$. Panel a shows the EULAG result, panel b shows the solution with the NH-IFS, panel c the hydrostatic IFS solution. Contour interval is $0.03\ ms^{-1}$. For comparison, panel d shows the IFS solution for the linear LS2 case (contour interval $0.015\ ms^{-1}$). The vertical axis is pressure in hPa.

drag results are reasonably close to the analytic solution; compare also to Fig. 9 in Grubišić and Smolarkiewicz (1997). The linear analytic solution is essentially hydrostatic, and both nonhydrostatic models correctly recover the hydrostatic balance on the reduced-size sphere.

Vertical cross-sections at the equator of vertical velocity in the LS2 run at equilibrium (not shown) compare well between all three models. However, the steady state is reached later with the IFS than with EULAG, as already indicated by the drag evolution in Fig. 10. Panel a in Fig. 12 shows the corresponding vertical vorticity in the horizontal plane at $0.94z_c$ after $t^* = 28.8$ for EULAG. Panels b and c show solutions from the hydrostatic IFS and the NH-IFS, respectively. While in EULAG the physically observable (locally Cartesian) vorticity components are evaluated at each grid point of the model domain, by accounting formally for all the metric terms (Smolarkiewicz and Prusa, 2005), in the IFS the component normal to constant model levels is used. The latter is routinely computed in the IFS at every time-step during the direct spectral transforms, whereby the local wind components — in the semi-Lagrangian formalism — are transformed into a spectral representation of vorticity and divergence — used in the semi-implicit solution procedure. In the LS2 case, the vorticity component normal to $\eta = $ const. closely approximates the vertical vorticity. Best comparison with EULAG has been found if the nearest model level equivalent to $0.94z_c$ is shifted upward by $3dz$. Cross-sections of vertical velocity (Fig. 13d) indicate, that the damping to zero of vertical velocity amplitude at the critical level occurs slightly higher up in the IFS than in EULAG, despite the same prescribed height of the critical level. The imbalanced impulsive initial condition employed in the IFS calculations may be contributing to this disparity. In the EULAG solution a slightly poleward directed flow is noted together with a more elongated shape of the vorticity contour and a third contour maximum in the near equatorial region. Apart from these relatively minor differences, the results of both global models are in agreement with the limited-area solutions presented in Fig. 14 b,c in Grubišić and Smolarkiewicz (1997). Vertical cross-sections of vertical vorticity obtained with EULAG show essentially zero vorticity above the critical level in the vicinity of the mountain; see Fig. 14a in Grubišić and Smolarkiewicz (1997). However, the IFS results show weak but non-zero magnitude of vertical vorticity above z_c over the mountain (not shown).

In the nonlinear case (LS5) the solution is less trapped below the critical level (Grubišić and Smolarkiewicz, 1997), and both the IFS and EULAG capture these effects similarly. Panel a in Fig. 13 represents the vertical velocity cross-section after $t^* = 43$ for the EULAG model results, panel b and panel c show the results for the nonhydrostatic and the hydrostatic IFS, respectively. Panel d shows the vertical velocity for the linear LS2 case and the same critical level height. A comparison with a lower vertical resolution simulation (not shown) indicates that the behaviour is more influenced by vertical resolution than by the choice of the hydrostatic or nonhydrostatic model equations for this case. Note however, that this is not a priori obvious, since vertical and horizontal length scales in the nonlinear resolved motions are similar, hence this represents a nonhydrostatic regime. Indeed a closer examination shows that the hydrostatic solution is noisier and oscillatory below the critical level and in the lee of the mountain. This is reminiscent of the breakdown of the (hydrostatic) shallow water flow assumption for the critical flow case of a hydraulic jump, illustrated in Wedi and Smolarkiewicz (2004). The drag history in Fig. 14 reaches an equilibrium state for the EULAG simulation approximately after $t^* = 43$. The analytic solution of the linear case (LS2) is shown for reference. The amplitude of the normalised drag varies more strongly between the models. Both the NH-IFS and the hydrostatic IFS model (shown until $t^* = 43$) give relatively larger drag compared to the nonhydrostatic EULAG solution at that time. Until $t^* = 10$ the resulting drag agrees more closely between EULAG and the IFS; then the IFS solution oscillates around the EULAG value and slowly converges towards the same solution (normalised drag 1.14 at $t^* = 168$). In Grubišić and Smolarkiewicz (1997) the drag history is only shown to $t^* = 18$, where the drag evolution reaches a normalised maximum value of 1.25 in agreement with the EULAG solution presented here. The NH-IFS reaches a normalised maximum drag value of 1.6.

The solution departure of the hydrostatic and the nonhydrostatic results is illustrated for the nonlinear LS5
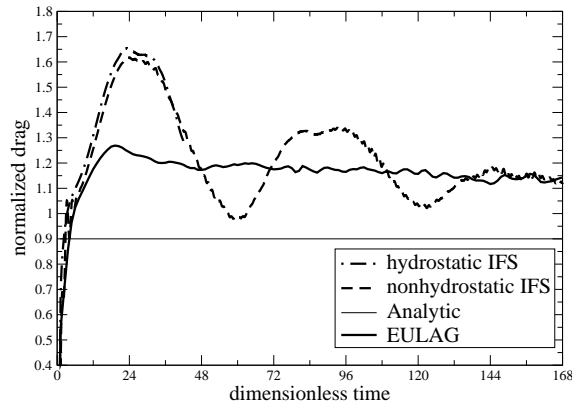
Figure 14: Comparison of the normalised drag history for the NH-IFS and the hydrostatic IFS, and EULAG for the nonlinear critical flow past a three-dimensional hill on the sphere (LS5). The linear analytic solution (LS2 case) is given by the thin solid line. The dashed line is for the NH-IFS, the solid thick line denotes EULAG, and the dot-dashed line shows the hydrostatic IFS solution.
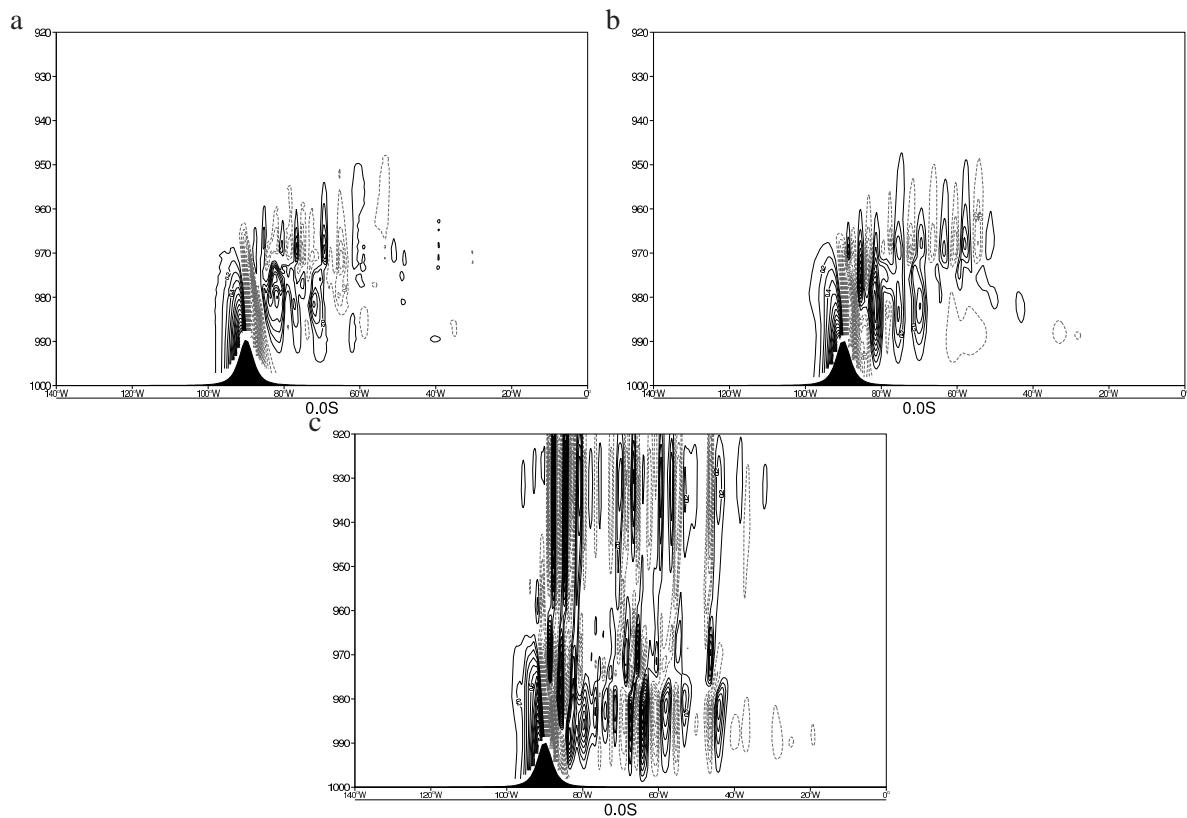

Figure 15: Vertical velocity from the LS5 case at $t^* = 216$ with $U_0/NL_\lambda = 1$. Panel a shows the EULAG result, panel b shows the solution with the NH-IFS, panel c the hydrostatic IFS solution. Contour interval is $0.2\ ms^{-1}$. The vertical axis is pressure in hPa.

case with three simulations for a narrower mountain, such that $U_0/NL_\lambda = 1$. To keep the ratio $L_\lambda/dx \equiv 4$, the horizontal resolution is enhanced to $dx = 250$ m by reducing the radius to $a = 20.3718$ km. The resulting nonhydrostatic solution is trapped below the critical level for both models (Fig. 15a-b). The structure of the vertical velocity in the lee of the mountain and in the vicinity of the critical level is consistent with the formation of a homogeneous mixed layer — resulting from convective and shear instabilities — that acts as a perfect reflector to all incoming waves; Grubišić and Smolarkiewicz (1997) and references therein. In contrast, the hydrostatic model result (Fig. 15c) evinces a strong wave response above the critical layer. The corresponding zonal drag is overestimated by 25 percent compared to the nonhydrostatic solutions, which are similar to the linear analytic solution (Fig. 16). Thus, in terms of the drag, the linear analytic solution also provides the asymptotic limit for high resolution fully nonlinear nonhydrostatic simulations.
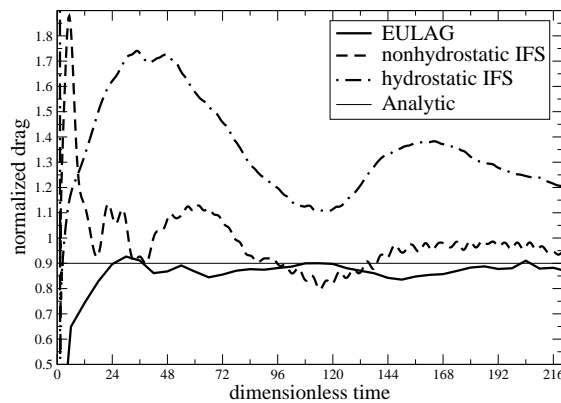

Figure 16: Comparison of the zonal drag history for the NH-IFS and the hydrostatic IFS, and EULAG for the LS5 case with $U_0/NL_\lambda = 1$. The linear analytic solution is denoted by the thin solid line. The dashed line is for the NH-IFS, the solid thick line denotes EULAG and the dot-dashed line shows the hydrostatic IFS solution.

3.6   Held-Suarez climate

The synoptic- and planetary-scale simulations presented in this section evaluate the influence of the dynamical core formulation on an idealised 'climate' state on the sphere, while the spectrum of the resolved scales is shifted with decreasing radii towards a smaller physical wavelength. It thus enables the study of basic atmospheric processes on the sphere and their numerical realisability with increasing yet affordable resolution. Planetary simulations on reduced-size spheres have been successfully demonstrated in Smolarkiewicz et al. (1999).

In the test cases discussed in previous sections near analytic results can be equivalently achieved on reduced-size planets with no further rescaling. However, since the planetary climate crucially depends on the evolution of Rossby waves, and it is our desire to keep such evolution Earth like, the Rossby number $Ro \equiv U/2\Omega L$ (assuming a characteristic horizontal speed U and length scale $L \sim a$) is kept constant in the following test case, which facilitates an intercomparison with the Earth's climate. In particular, it is important for maintaining the relative latitudinal positions of zonal jet cores, which establish in sufficiently long simulations (Held and Hou, 1980).

For Held-Suarez climate simulations a friction term $-k_v\mathbf{v}$ is added on the right-hand side of the horizontal momentum equations and a relaxation term $-k_T(T - T_{eq})$ is added on the right-hand side of the thermodynamic

equation. For completeness the Held-Suarez setup is summarised below, see Held and Suarez (1994) for details:

$$T_{eq} = \max\left\{200 \text{ K}, \left[315 \text{ K} - (\Delta T)_y \sin^2(\phi) \right. \right. \tag{14}$$

$$\left. \left. - (\Delta\theta)_z \log\left(\frac{p}{p_0}\right) \cos^2\phi \right] \left(\frac{p}{p_0}\right)^{\kappa}\right\}$$

$$k_T = k_a + (k_s - k_a)\cos^4\phi \ \max\left\{0, \frac{\sigma - \sigma_b}{1 - \sigma_b}\right\}$$

$$k_v = k_f \max\left\{0, \frac{\sigma - \sigma_b}{1 - \sigma_b}\right\}$$

$$k_f = 1 \text{ day}^{-1}, \ \ k_a = k_f/40, \ \ k_s = k_f/4,$$

$$(\Delta T)_y = 60 \text{ K}, \ \ (\Delta\theta)_z = 10 \text{ K}, \ \ \sigma_b = 0.7,$$

$$\text{day} = 2\pi/\Omega, \ \ p_0 = 1000 \text{ hPa}, \ \ \kappa = R/c_p.$$

With fixed Ro, reducing the radius of the planet implies an equivalent increase of the rotation rate and, thus, a corresponding increase in the frictional/heating time factors k_f, k_a, k_s. The setup is otherwise as described in Smolarkiewicz et al. (1999, 2001) for EULAG.

Simulations are performed for spheres with radii $a = (a_E, a_E/10, a_E/20)$ where $a_E = 6.371 \cdot 10^6$ m. The IFS is run with the operational set of 91 vertical levels and the top model level located at 0.01 hPa (model top at $p = 0$). In EULAG 40 vertical layers are used with a top-height fixed at 32 km. Both models start from identical initial conditions and use the same timestep, respective for the radius of the experiment, $\Delta t = 300, 30, 15$ s, chosen such as to keep the maximum Courant number ($a^{-1}(U_{max}\Delta t/\Delta\lambda)$) of both the IFS and EULAG simulations similar (close to 0.6) and minimising the difference in the truncation error; cf. section 6.1 in Durran (1999). The equivalent gridsizes of the simulations are 125, 12.5, and 6.25 km. The latter two are close to possible future resolutions at ECMWF but use only a fraction of the computational cost normally required for simulations at such fine resolution. Thus idealised simulations on reduced planets may be run at a cost comparable to the current high resolution forecast at ECMWF but with one order of magnitude higher resolution. This enables an in-depth evaluation of various features of the global model before such a high resolution is routinely affordable.

Figure 17 shows the solutions for the case of $a = a_E/10$. It compares the zonal mean zonal flow of the NH-IFS (panel a), the hydrostatic IFS (panel b), and EULAG (panel c) averaged over the integration period of 275 simulation days (skipping the first 10 simulation days). A simulation day is defined as the time period of one planetary rotation. The zonal jet positions and magnitudes in the zonally averaged solutions compare well in all simulations for different models and radii. Figure 18 compares the change of the zonally-averaged mean state for three different horizontal resolutions obtained with the NH-IFS and Fig. 19 for EULAG. In agreement with theoretical predictions there is remarkably little difference between the averaged solutions for each model. Despite differences in the upper boundary and the vertical coordinate the solutions agree closely. The asymmetry seen for example in Fig. 18b and Fig. 19b indicate a small equatorward shift of the southern hemispheric jet for both IFS and the EULAG simulation with $a = a_E/10$, showing that the zonal mean state does not reach a steady state after 275 simulation days.

Fig.20 shows the time-averaged horizontal kinetic energy $E = 0.5(u^2 + v^2)$ distribution against the total spherical harmonic wavenumber n for the NH-IFS and EULAG, each with radii $a = a_E$ and $a = a_E/10$. The horizontal kinetic energy spectrum remains nearly identical, if all numerical parameters (including for example horizontal diffusion as applied in IFS) are appropriately rescaled. The spectrum has been obtained by averaging in time over the last 100 simulation days. Notably, for both models small differences can be seen in the well-resolved range of total wavenumbers $6 - 20$ approximately[2], which are associated with the dominant midlatitude baro-

---

[2]The zonal and meridional physical wavenumbers, k and l, respectively, are related to the eigenvalues of the Helmholtz equation of
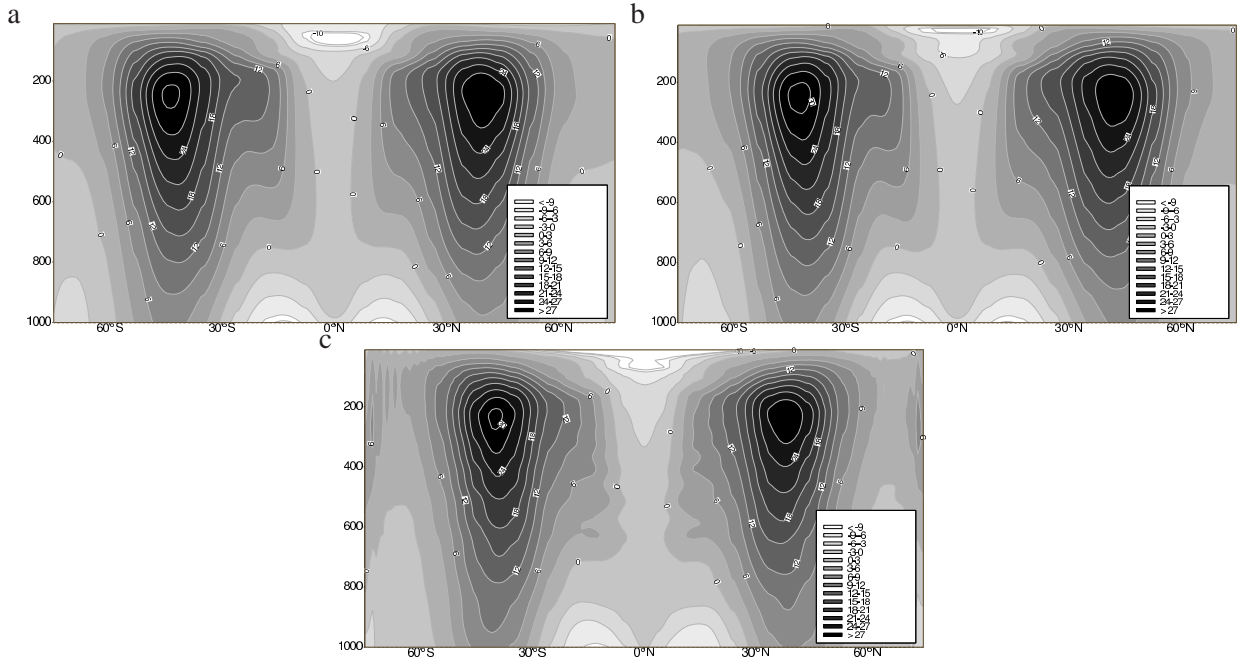
Figure 17: Held-Suarez dry climate simulation on the reduced-size sphere with $a = 0.1a_E$. Panel a-b show the zonal mean zonal flow for the NH-IFS and the hydrostatic IFS, respectively. Panel c shows the result for EULAG. Fields are averaged over 275 simulation days (defined as the time for one planetary rotation). The vertical axis is pressure in hPa.
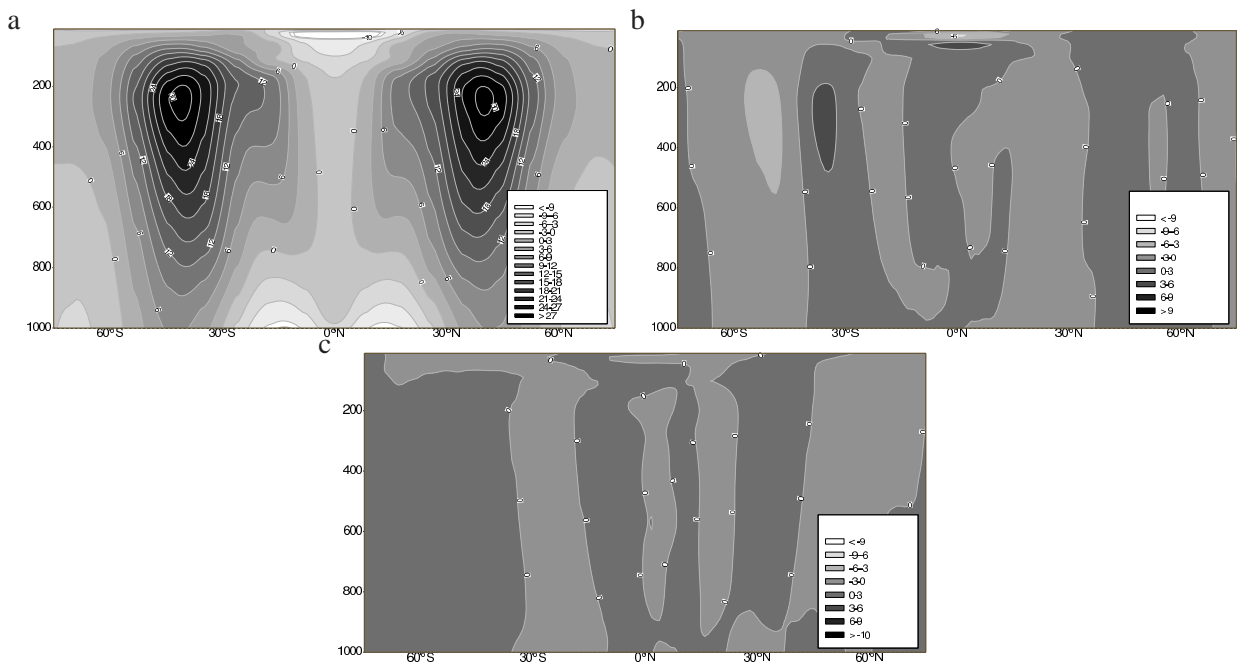

Figure 18: NH-IFS Held-Suarez dry climate simulations on the sphere with (a) horizontal resolution $dx \approx 125$ km ($a = a_E$), b) the difference between the $dx \approx 125$ km and the $dx \approx 12.5$ km ($a = a_E/10$) simulation, and c) the difference between $dx \approx 125$ km and $dx \approx 6$ km ($a = a_E/20$). The zonal mean zonal flow is averaged over 275 simulation days.
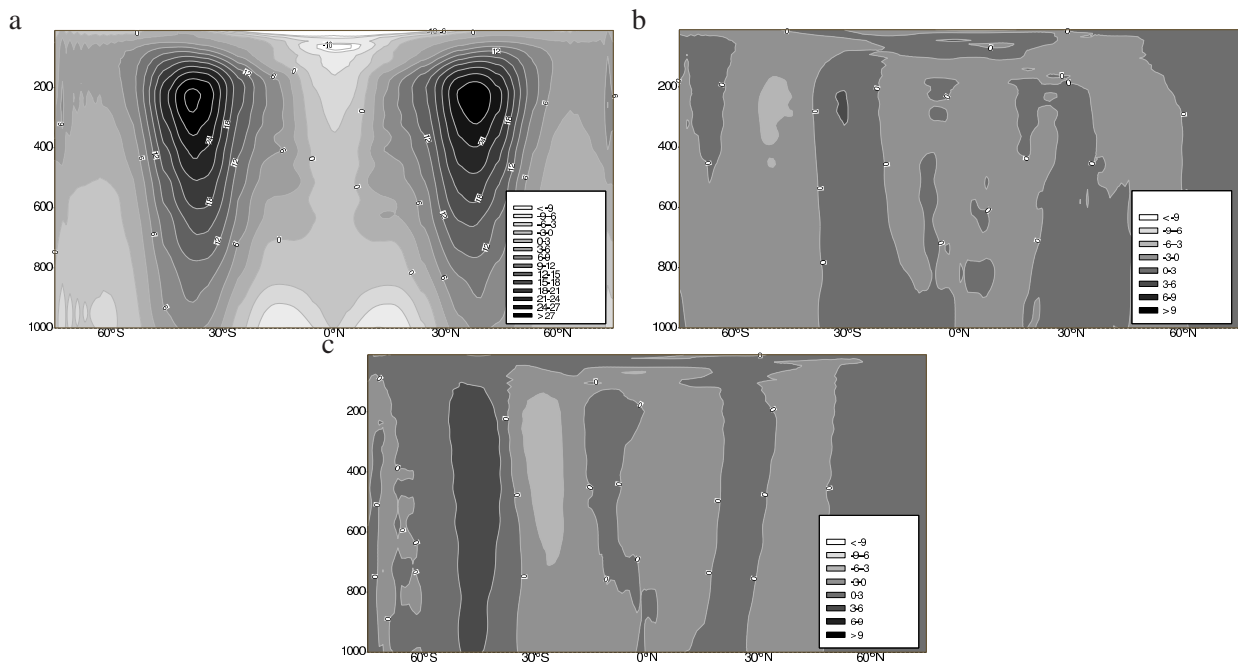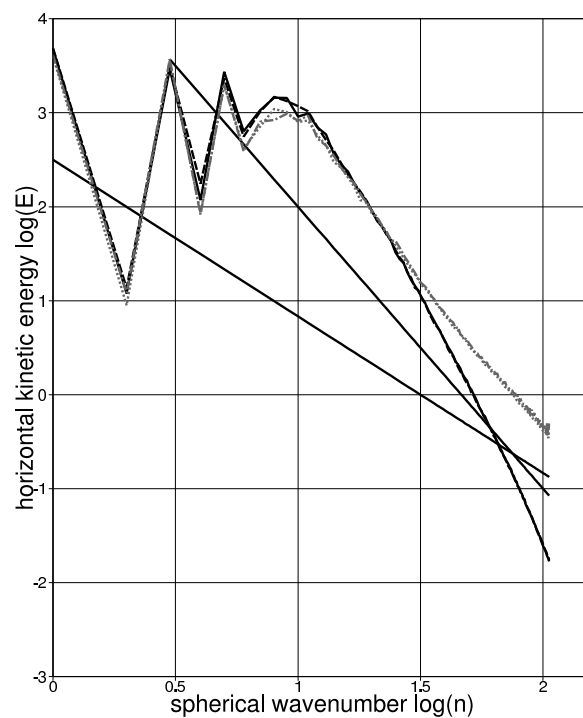
Figure 19: EULAG Held-Suarez dry climate simulations on the sphere with (a) horizonal resolution $dx \approx 125 \, km$ ($a = a_E$), b) the difference between the $dx \approx 125 \, km$ and the $dx \approx 12.5 \, km$ ($a = a_E/10$) simulation, and c) the difference between $dx \approx 125 \, km$ and $dx \approx 6 \, km$ ($a = a_E/20$). The zonal mean zonal flow is averaged over 275 simulation days.

Figure 20: A $\log_{10}$-$\log_{10}$ presentation of horizontal kinetic energy $[m^2 s^{-2}]$ at 200 hPa averaged over the last 100 simulation days for the IFS and the EULAG simulations with different Earth's radii. The abscissa shows the total spherical harmonic wavenumber n. The solid line denotes the IFS simulation with $a = a_E$, the dashed line is the IFS simulation with $a = a_E/10$; the grey dotted line denotes the EULAG simulation with $a = a_E$, and the grey dash-dotted line is the EULAG simulation with $a = a_E/10$. Wavenumber spectra $n^{-5/3}$ and n^{-3} have been added for reference.

clinic waves arising in the Held-Suarez climate. At radii $a = a_E$ and $a = a_E/10$ NH-IFS shows substantially higher amplitude compared to EULAG (maximal 24 percent difference) in the $6 - 20$ total wavenumber range, whereas EULAG shows significantly higher amplitude at total wavenumbers > 20, in particular at the tail end of the spectrum.

The richness and variability of the different solutions for the Held-Suarez test case — known for the intercomparison of its atmospheric zonal mean states — is further illustrated in Fig.21 and Fig.22. Figure 21 shows the temporal anomalies of 200 hPa zonal wind averaged between 30N-50N latitudes, a display method often used for the illustration of intraseasonal oscillations. The data has been lowpass filtered to attenuate all frequencies higher than $2\pi/10$ day^{-1}. The eastward propagation and the persistence of these anomalies in both models is sensitive to the diffusive character of the numerical solution (not shown), with more diffusion implying more persistent propagating anomalies (cf. Piotrowski et al. (2009)). Figure 22 shows for both models, the NH-IFS and EULAG, the power in frequency (cycles per simulation day $\equiv$ 1/period) and wavenumber space for 200 hPa zonal wind averaged between 30N and 50N. The two models show similar dominant wavenumbers but differences in both amplitude and frequency, albeit identical initial conditions, the same physical forcing and a similar zonally-averaged mean state. The spurious persistence of the anomalies and the differences in the spectra warrant further investigation, given the potential importance for medium range weather prediction and climate.
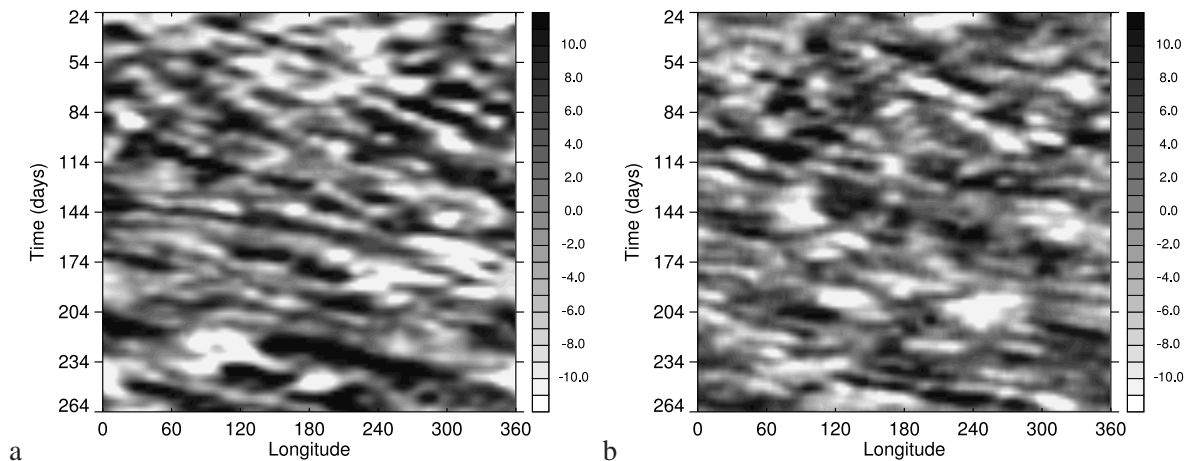

Figure 21: Hovmöller diagram of the temporal anomaly of 200 hPa zonal wind for 275 simulation days averaged between 30N and 50N for a) the NH-IFS and b) EULAG on the reduced-size sphere ($a = a_E/10$). Contours are in ms^{-1}.

3.7 Medium-range NH-IFS performance and model climate

The medium-range forecast performance of the NH-IFS at hydrostatic resolutions is assessed in comparison to the hydrostatic IFS. All NH-IFS experiments shown use the GWADV-NH option. However, earlier experiments indicate insignificant differences in performance of the NH-IFS with or without the GWADV-NH option in medium-range forecasts at hydrostatic scales. Notably, the NH-IFS simulations presented here use finite-difference discretisation in the vertical, whereas the hydrostatic control simulations use the finite-element scheme. Both models employ the implicit treatment of the Coriolis force as it leads to slightly better forecast scores and formally minimises the departure from "inertness" in the two-time-level numerical discretisation.

The initial conditions for the two additional nonhydrostatic variables are obtained by assuming a hydrostatically balanced vertical motion together with a pressure field that is free of elastic perturbations, cf. Bénard et al.

the spherical harmonic functions and thus to the total spherical wavenumber n via $(k^2 + l^2) = n(n+1)/a^2$ (Phillips, 1990).
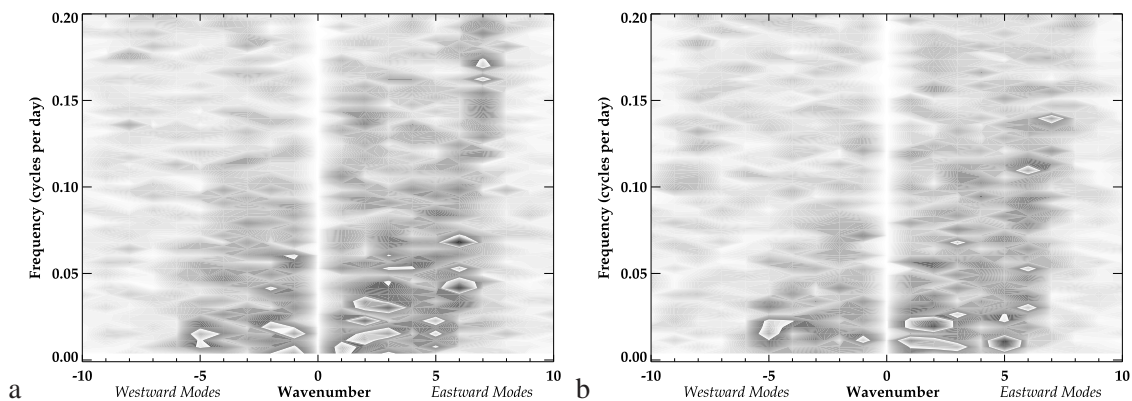
Figure 22: Power in frequency (cycles per day) and wavenumber space for 200 *hPa zonal wind averaged between 30N and 50N for a) the NH-IFS and b) EULAG on the reduced-size sphere (a = a_E/10).*

(2009).

Scores from 10-day forecasts at T_L799 and at T_L1279 with 91 vertical levels are shown in Fig. 23 and Fig. 24, respectively. Both hydrostatic and nonhydrostatic forecasts were run with the same timestep (the default for the H-IFS): $\Delta t = 720$ s at T_L799 and $\Delta t = 450$ s at T_L1279. The left figures in Fig. 23 and Fig. 24 show anomaly correlation and the right figures root mean square error for 500 hPa geopotential height for the extratropical northern hemisphere (panel a) and southern hemisphere (panel b) from 10-day simulations for different initial dates spread over the period 2007-2008. Panel c shows absolute correlation and root mean square error for the 200 hPa winds in the tropics. All forecasts are verified against the operational analysis. The forecasts at T_L1279 were run with model version $CY35R1$ and those at T_L799 with $CY35R2$.

The differences in scores between the nonhydrostatic and hydrostatic runs are small and not significant. This is also the case for other parameters, areas and heights in the troposphere. The only significant difference is in the stratosphere, where the hydrostatic simulations are consistently better. This difference is explained by the difference in vertical discretisation schemes used in the two models. By default the H-IFS is using the vertical finite-element discretisation (VFE) while the NH-IFS a vertical finite-difference discretisation (VFD), and, as was noted in Untch and Hortal (2004) with the H-IFS, the former gives better stratospheric forecasts. When both models are run with their respective VFD discretisations, the scores in the stratosphere are very similar, but inferior to those of the H-IFS with VFE discretisation. However, if the "intermediate" VFE discretisation, described in the Appendix, is used in the NH-IFS, its stratospheric scores are improved and compare well with those of the H-IFS with VFE discretisation.

Additional diagnostics on the position of the departure points of the semi-Lagrangian trajectories near the model surface and the model top shown that both models are having occasional problems at individual points near the surface over steep orography with excessive vertical velocities that lead to the semi-Lagrangian trajectories originating from outside of the model domain. However, for the NH-IFS this happens up to four times more often than for the H-IFS at T_L799 and gets worse with increasing horizontal resolution. The stability of the semi-implicit scheme in the NH-IFS is controlled via the acoustic reference temperature chosen to be $T_{ra} = 75$ K and the standard reference temperature controlling the propagation of gravity waves $T_r = 350$ K (same as for H-IFS) (see also section 3.1). For the semi-implicit reference pressure p_r a smaller value of 850 hPa is chosen for stability than in the H-IFS ($p_r = 1000$ hPa). It is noted, that the empirically determined range of stability for T_{ra} of $50 < T_{ra} < 100$ — guided by the experiments in section 3.1 — is quite restrictive.

Additionally two 10-day simulations have been run with T_L2047 (10km grid-size) and 91 vertical levels. The results indicate a stable integration and a similar evolution of the rms-error and anomaly-correlation of the

Figure 23: Comparison of the $T_L 799$ simulations using the H-IFS and the NH-IFS model formulation (CY33R2). Panel a and b show the average over 41 days of 500 hPa geopotential height root mean square error and anomaly correlation for the northern and the southern hemisphere, respectively. Panel c shows the absolute correlation and root mean square error of the 200 hPa winds in the tropics.
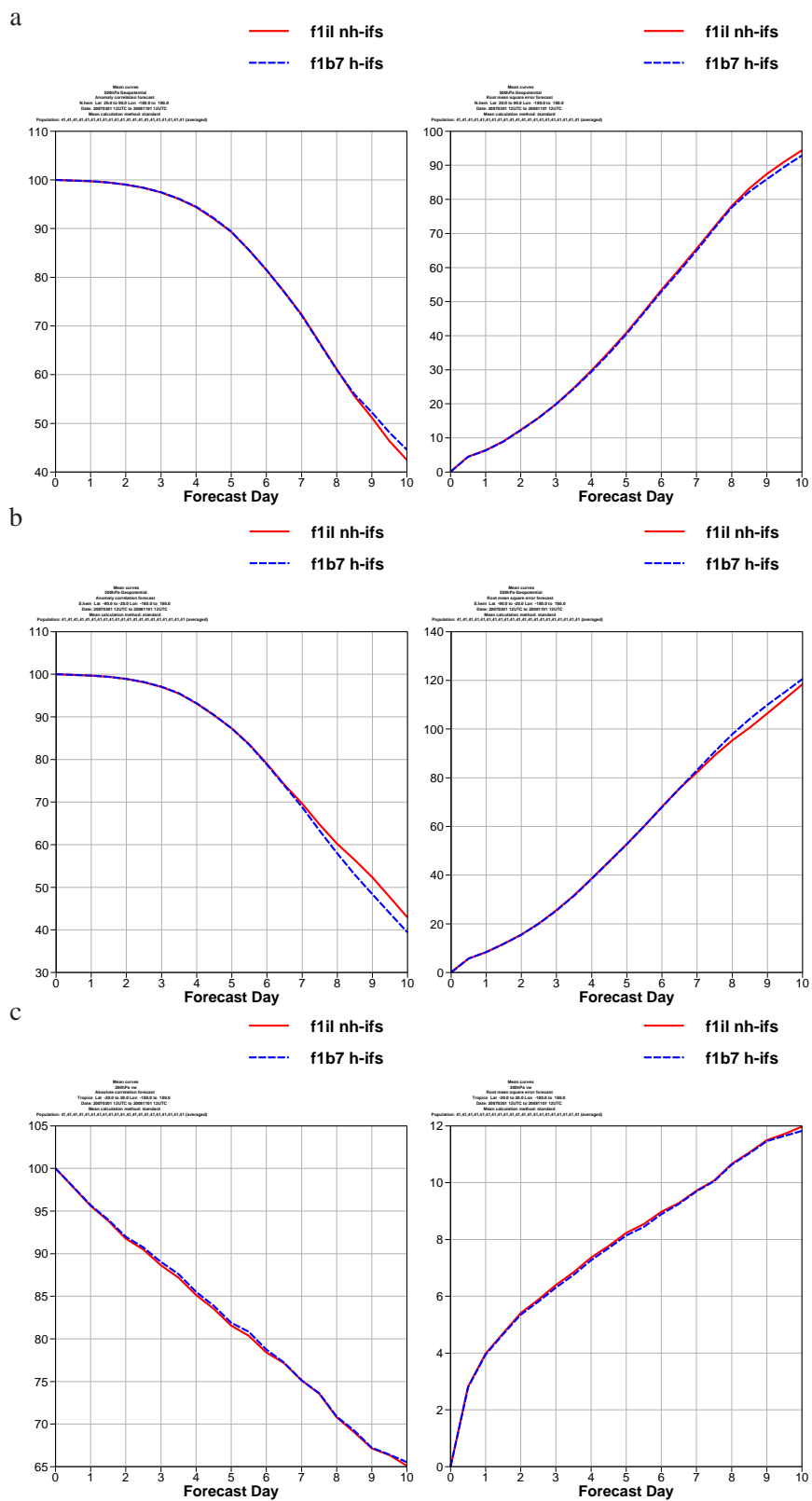
a

b

c

Figure 24: Comparison of the T_L1279 simulations using the H-IFS and the NH-IFS model formulation (CY35R1). Panel a and b show the average over 49 days of 500 hPa geopotential height root mean square error and anomaly correlation for the northern and the southern hemisphere, respectively. Panel c shows the absolute correlation and root mean square error of the 200 hPa winds in the tropics.
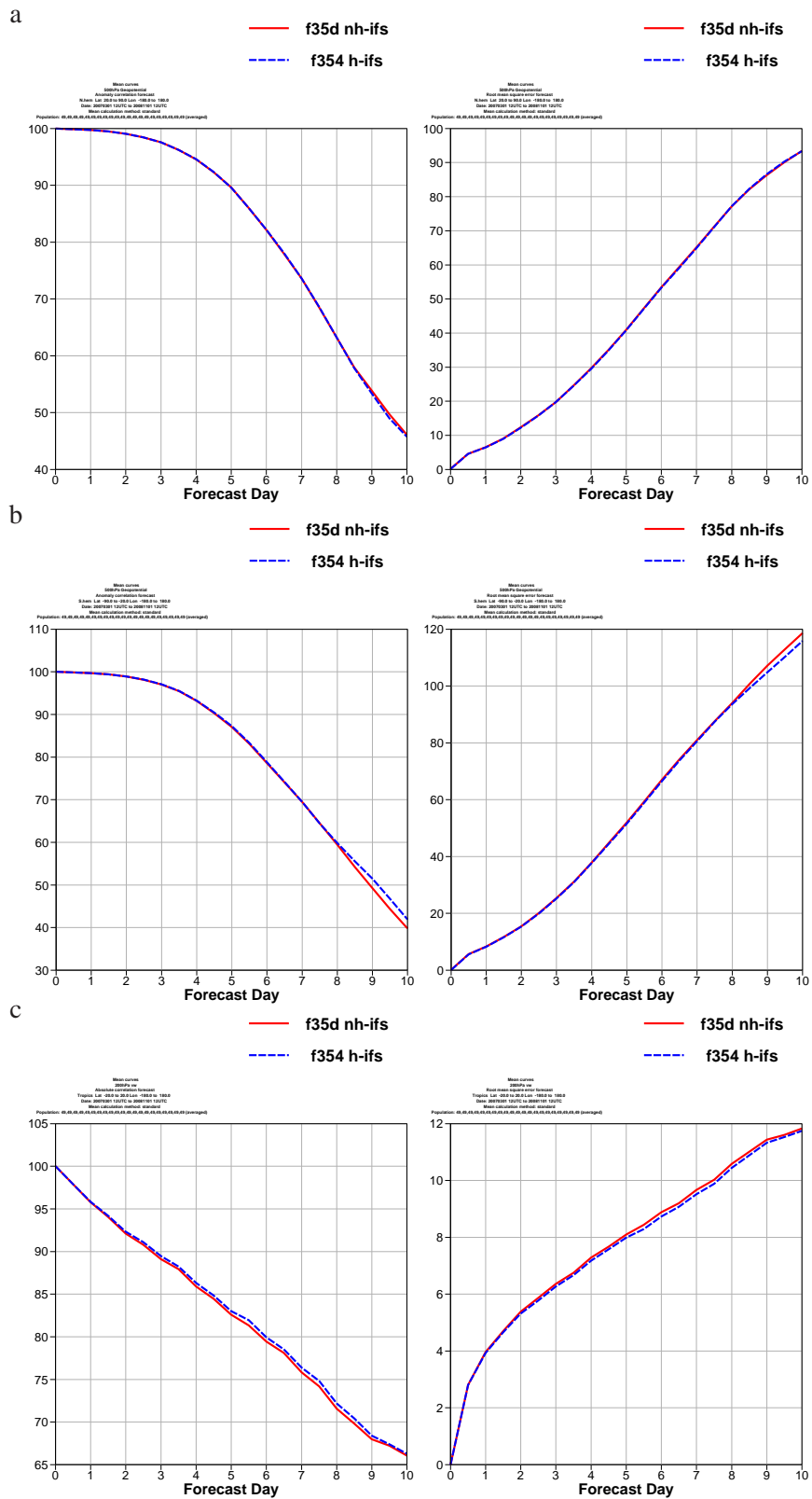
500 hPa geopotential height compared to the corresponding $T_L 1279$ simulations, for both H-IFS and NH-IFS. Precipitation patterns are very similar upto day 6 of the forecasts. Although not believed to be significant, if a fine contour interval $< 2mm/day$ is chosen, different wave patterns can be seen at day 6. In the nonhydrostatic $T_L 2047$ runs the problem of trajectories outside the model domain is increased, with a ratio $15 : 1$ compared to the corresponding H-IFS simulation.

The sensitivity of the model climate to the model formulation is studied using a 4-member ensemble of 13-month-long integrations with cycle $32r3$ using the atmospheric component of the ECMWF Integrated Forecasting System only. A horizontal resolution of $T_L 159$ is used with 91 levels in the vertical. Observed sea surface temperatures are prescribed as lower boundary conditions. Forecasts are started 1 August 2000 00UTC and shifted by 30 hours for each subsequent ensemble member. The timestep used is $\Delta t = 3600s$. The tropospheric model climate in hydrostatic and non-hydrostatic simulations is found to be nearly identical and the differences manifest themselves only in a stratospheric temperature bias related to the vertical discretisation.

A number of similar experiments have been conducted in the rotated and stretched (factor $c = 2.4$) ARPEGE framework (Courtier and Geleyn, 1988; Courtier et al., 1991; Yessad and Bénard, 1996) with $T_L 538$ and with 60 vertical levels. (Note that the ARPEGE vertical level distribution differs from the IFS 60 levels.) In this configuration $ND4SYS = 1$ is used and the physics package is called at the beginning of the time-step. The option to compute the Coriolis force implicitly is not available for the stretched and rotated system. Notably, the instability over steep orography found with the NH-IFS setup (originating from the discretisation of the $\mathscr{X}$-term) does not occur with the ARPEGE setup. Otherwise, similar results with respect to stability and accuracy are obtained when compared to the corresponding ARPEGE hydrostatic version.

3.8   Computational cost

The computational cost of the NH-IFS model is related to the numerical stability of the iterative centred-implicit (ICI) scheme. If the same timestep as used for the hydrostatic model is desired, the nonhydrostatic simulations require at least one iteration ($N_{iter} = 1$) of the ICI scheme to be stable. This means that the dynamics computations are executed twice per timestep, the physical parametrizations are called only once at the end of the iteration over the dynamics. For the $T_L 159$ model climate simulations this results in a 35 percent computational cost increase compared to the hydrostatic model (in the current operational configuration). The cost increase can be reduced to approximately 24 percent if $N_{iter} = 0$, i.e. the standard (un-iterated) semi-implicit scheme is used, and the timestep is optimally reduced to ensure stability. While comparable results are obtained at this low resolution, this is no longer the case at higher resolutions. The cost increase in the 10-day $T_L 799$ simulations is approximately 70 percent, at $T_L 1279$ it is about 80 percent, and at $T_L 2047$ 106 percent. Figure 25 shows a breakdown of the cost for the different parts of the model (dynamics in gridpoint space, computations in spectral space, spectral transforms, physical parametrizations and other computations) at $T_L 2047$ for NH-IFS and H-IFS. While the absolute cost of the physical parametrizations remains the same, the cost of the dynamics (gridpoint and spectral-space computations) and in particular the cost of the spectral transforms grow substantially because of the iteration over the dynamics in the ICI scheme. As a result the overall balance of the computational costs in the IFS shifts. Figure 26 shows the relative contribution to the total cost for the hydrostatic IFS and NH-IFS at $T_L 2047$. In the hydrostatic model 39 percent of the time is spent in the physical parametrizations, whereas in the NH-IFS model with one iteration of the ICI scheme only 16.9 percent of the cost are apportioned to the physics.

A reduction in cost can be made by computing the semi-Lagrangian trajectory, and thus the departure point interpolations, only once. While this removes the benefit of updating the trajectory with information due to the previous iteration, the impact on the scores is neutral and the cost saving is approximately 10 percent independent of resolution (same saving at $T_L 799$ and at $T_L 2047$). However, numerical noise develops in the
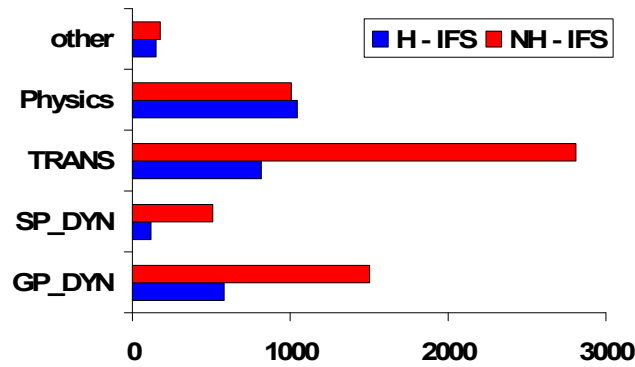
Figure 25: Comparison of the cost of the NH-IFS against the hydrostatic IFS at T_L2047 resolution: breakdown of the to-tal cost into the contributions from the gridpoint dynamics (GP_DYN), the spectral computations (SP_DYN), the spectral transforms (TRANS), the physical parametrizations (PHYSICS), and the remaining computations (other) such as postpro-cessing and diagnostics. The horizontal axis shows elapsed time in seconds for the different parts of the model in a 5-day forecast on 2048 processors.
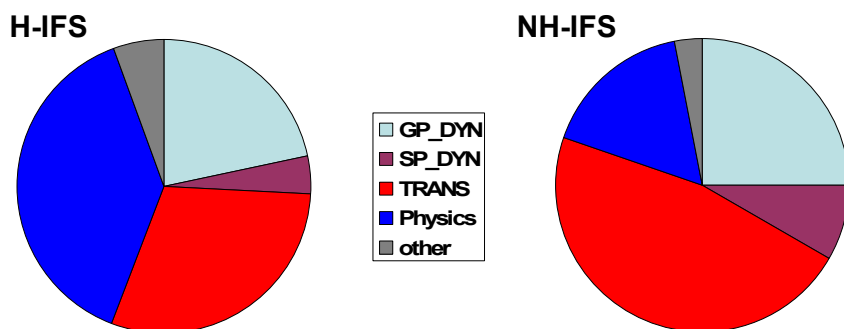

Figure 26: Relative cost of the individual contributions to the total computation time for the hydrostatic IFS (left) and the NH-IFS (right).

stratosphere with this formulation. The cause for this instability is not well understood and requires further investigation.

Further reductions in cost may be possible if some a priori filtering of acoustic modes enhances the stability properties of the NH-IFS model and potentially eliminates the need for an iterative procedure. In addition, advances in the speedup of the spectral transforms (fast Legendre transforms) may be sought.

4   Discussion and conclusions

The NH dynamical core developed by the ALADIN partnership (Bubnová et al., 1995) (ALADIN, 1997) and made available by Meteo-France in the global IFS/ARPEGE model (Yessad, 2008) has been tested in the ECMWF global modelling environment and its performance has been assessed in terms of accuracy, stability and cost by comparing to the Centre's operational hydrostatic model (H-IFS) at hydrostatic resolutions and to LES benchmarks at ultra high resolutions where nonhydrostatic phenomena are resolved.

The test cases studied at nonhydrostatic resolutions have shown that the NH-IFS captures the essential nonhydrostatic effects and, apart from relatively minor differences,the NH-IFS solution compares quantitatively well with Cartesian-domain analytic solutions and LES benchmarks.

The forecast quality obtained with the NH-IFS in global medium-range and seasonal simulations at hydrostatic resolutions is very similar to the quality obtained with the H-IFS. This was, however, only achieved after upgrading the original NH IFS/ARPEGE model with two options available and used by default in the hydrostatic IFS: implicit computation of the Coriolis force and a finite-element discretisation in the vertical, albeit only an "intermediate" finite-element version (see Appendix for details).

Based on the performance of the NH-IFS model in terms of accuracy, it can be concluded that the NH-IFS dynamical core is a possible choice for future, globally-uniform high resolution applications at ECMWF. An assessment of moist simulations with the NH-IFS model at nonhydrostatic scales is ongoing. In the hydrostatic regime, forecasts of moist quantities with the NH-IFS and H-IFS in medium- and seasonal-range are nearly identical up to ≈ 10 km grid-length, using the ECMWF physical parametrization package "as is". At cloud-resolving resolutions, various aspects of moist dynamics need further assessment, in particular, the coupling of the physical parametrizations to the NH dynamical core and the projection of diabatic heating on both pressure and temperature, the need for moist-conservative variables for advection, and the efficacy of the semi-Lagrangian advection scheme per se.

The numerical stability of the NH-IFS has been assessed for global weather applications at full complexity with long timesteps (as used for the H-IFS) and horizontal grid-sizes up to ≈ 10 km. At least one iteration of the iterative centred-implicit scheme is required to stabilise the NH integrations with such long timesteps. This means the dynamical core computations are executed twice per timestep (the physics package is called only once), leading to a very substantial increase in cost compared to the hydrostatic model, e. g. for 10-day forecasts at $T_L 799$ (25km grid-size) the cost increase is about 70 percent, while at $T_L 2047$ (10km) the cost doubles. Therefore, the NH-IFS is not competitive with the H-IFS for hydrostatic scale applications. If efforts directed at reducing substantially the cost of the NH-IFS prove to be unsuccessful, the H-IFS will have to be maintained and used for the Centre's low and medium resolution applications in the future, e.g. in the inner loops of the 4D-Var assimilation system. However, maintaining both models does not require an unduly large effort because the two dynamical cores share large parts of the code, since the NH model is designed as an extension to the existing hydrostatic model (Bubnová et al., 1995). It would, however, be desirable to have the same dynamical core for all applications at all scales. For this the efficiency of the NH dynamical core will have to be improved substantially, a demanding project which will require a considerable amount of research.

References

ALADIN (1997). The ALADIN project: Mesoscale modelling seen as a basic tool for weather forecasting and atmospheric research. *WMO Bull. 46*, 317–324.

Bénard, P. (2004). On the use of a wider class of linear systems for the design of constant-coefficients semi-implicit time schemes in NWP. *Mon. Weather Rev. 132*, 1319–1324.

Bénard, P., R. Laprise, J. Vivoda, and P. Smolíková (2004). Stability of leapfrog constant-coefficients semi-implicit schemes for the fully elastic system of Euler equations: Flat-terrain case. *Mon. Weather Rev. 132*, 1306–1318.

Bénard, P., J. Mašek, and P. Smolíková (2005). Stability of leapfrog constant-coefficients semi-implicit schemes for the fully elastic system of Euler equations: case with orography. *Mon. Weather Rev. 133*, 1065–1075.

Bénard, P., J. Vivoda, J. Mašek, P. Smolíková, K. Yessad, R. Brozkova, and J.-F. Geleyn (2009). Dynamical kernel of the ALADIN-NH spectral limited-area model: formulation and sensitivity experiments. *Mon. Weather Rev.*. submitted.

Bubnová, R., G. Hello, P. Bénard, and J.-F. Geleyn (1995). Integration of the fully elastic equations cast in the hydrostatic pressure terrain-following coordinate in the framework of the ARPEGE/Aladin NWP system. *Mon. Weather Rev. 123*, 515–535.

Catry, B., J.-F. Geleyn, M. Tudor, P. Bénard, and A. Trojáková (2007). Flux-conservative thermodynamic equations in a mass-weighted framework. *Tellus 59A*, 71–79.

Courtier, P., C. Freydier, J.-F. Geleyn, F. Rabier, and M. Rochas (1991). The ARPEGE project at Météo-France. In *Proc. 1991 Seminar on Numerical Methods in Atmospheric Models II*, Reading, UK, pp. 193–231. Eur. Cent. For Medium-Range Weather Forecasts.

Courtier, P. and J.-F. Geleyn (1988). A global model with variable resolution. application to the shallow water equations. *Q.J.R. Meteorol. Soc. 114*, 1321–1346.

Daley, R. (1991). *Atmospheric data analysis*. Cambridge, New York: Cambridge University Press.

Durran, D. R. (1999). *Numerical methods for wave equations in geophysical fluid dynamics*. New York: Springer-Verlag.

ECMWF (2000). *Proc. ECMWF Workshop on Developments in numerical methods for very high resolution global models*, Workshop proceedings, Reading, UK. ECMWF.

Geleyn, J.-F. (2005). New findings about the orographic chimney problem' in aladin-nh dynamical core and tentative conclusions for the code policy. http://www.rclace.eu.

Grabowski, W. W. and P. Smolarkiewicz (1990). Monotone finite difference approximations to the advection-condensation problem. *Mon. Weather Rev. 118*, 2082–2097.

Grubišić, V. and P. K. Smolarkiewicz (1997). The effect of critical levels on 3d orographic flows: Linear regime. *J. Atmos. Sci. 54*, 19431960.

Held, I. and A. Hou (1980). Nonlinear axially symmetric circulations in a nearly inviscid atmosphere. *J. Atmos. Sci. 37*, 515–533.

Held, I. and M. Suarez (1994). A proposal for the intercomparison of the dynamical cores of atmospheric general circulation models. *Bull. Am. Meteorol. Soc. 73*, 1825–1830.

Hundertmark, T. and S. Reich (2007). A regularization approach for a vertical slice model and semi-Lagrangian Störmer-Verlet time-stepping. *Q.J.R. Meteorol. Soc. 133*, 1575–1587.

Keller, T. L. (1994). Implications of the hydrostatic assumption on atmospheric gravity waves. *J. Atmos. Sci. 51*, 1915–1929.

Klemp, J. B., J. Dudhia, and A. D. Hassiotis (2008). An upper gravity-wave absorbing layer for NWP applications. *Mon. Weather Rev. 136*, 39874004.

Klemp, J. B. and D. K. Lilly (1978). Numerical simulation of hydrostatic mountain waves. *J. Atmos. Sci. 35*, 78–107.

Klemp, J. B., W. C. Skamarock, and O. Fuhrer (2003). Numerical consistency of metric terms in terrain-following coordinates. *Mon. Weather Rev. 131*, 1229–1239.

Kuang, Z., P. Blossey, and C. Bretherton (2005). A new approach for 3d cloud-resolving simulations of large-scale atmospheric circulation. *Geophys. Res. Lett. 32*(L02809), 1–4.

Landau, L. D. and E. M. Lifschitz (2004). *Fluid Mechanics*. Amsterdam: Elsevier.

Laprise, R. (1992). The Euler equations of motion with hydrostatic pressure as an independent variable. *Mon. Weather Rev. 120*, 197–207.

Phillips, N. A. (1990). Dispersion processes in large scale weather prediction. *WMO Bulletin* (700), 1–126. Sixth IMO lecture.

Piotrowski, Z. P., P. K. Smolarkiewicz, S. P. Malinowski, and A. Wyszogrodzki (2009). On numerical realizability of thermal convection. *J. Comput. Phys. 228*, 6268–6290.

Prusa, J. M., P. K. Smolarkiewicz, and A. A. Wyszogrodzki (2008). EULAG, a computational model for multiscale flows. *Comput. Fluids 37*, 1193–1207.

Ritchie, H., C. Temperton, A. Simmons, M. Hortal, T. Davies, D. Dent, and M. Hamrud (1995). Implementation of the semi-Lagrangian method in a high resolution version of the ECMWF forecast model. *Mon. Weather Rev. 123*, 489–514.

Robert, A. (1993). Bubble convection experiments with a semi-implicit formulation of the Euler equations. *J. Atmos. Sci. 50*, 1865–1873.

Robert, A., J. Henderson, and C. Turnbull (1972). An implicit time integration scheme for baroclinic models of the atmosphere. *Mon. Weather Rev. 100*, 329–335.

Schär, C., D. Leuenberger, O. Fuhrer, D. Lüthi, and C. Girard (2002). A new terrain-following vertical coordinate formulation for atmospheric prediction models. *Mon. Weather Rev. 130*, 2459–2480.

Smolarkiewicz, P. K., V. Grubišić, L. G. Margolin, and A. A. Wyszogrodzki (1999). Forward-in-time differencing for fluids: Nonhydrostatic modelling of fluid motions on a sphere. Proc. 1998 Seminar on Recent Developments in Numerical Methods for Atmospheric Modelling, Reading, UK, pp. 21–43. Eur. Cent. For Medium-Range Weather Forecasts.

Smolarkiewicz, P. K., L. G. Margolin, and A. A. Wyszogrodzki (2001). A class of nonhydrostatic global models. *J. Atmos. Sci. 58*, 349–364.

Smolarkiewicz, P. K. and J. M. Prusa (2005). Towards mesh adaptivity for geophysical turbulence: Continuous mapping approach. *Int. J. Numer. Methods Fluids 47*, 789–801.

Smolarkiewicz, P. K. and J. Szmelter (2008). An mpdata-based solver for compressible flows. *Int. J. Numer. Methods Fluids 56*, 1529–1534.

Temam, R. (2006). Suitable initial conditions. *J. Comput. Phys. 218*, 443–450.

Temperton, C. (1997). Treatment of the Coriolis terms in semi-Lagrangian spectral models. In *The Andre Robert Memorial Volume*, pp. 293–302. Canadian Meterological and Oceanographical Society.

Temperton, C., M. Hortal, and A. Simmons (2001). A two-time-level semi-Lagrangian global spectral model. *Q.J.R. Meteorol. Soc. 127*, 111–127.

Temperton, C. and A. Simmons (1997). Stability of a two-time-level semi-implicit integration scheme for gravity wave motion. *Mon. Weather Rev. 125*, 601–615.

Untch, A. and M. Hortal (2004). A finite-element scheme for the vertical discretization of the semi-lagrangian version of the ecmwf forecast model. *Q.J.R. Meteorol. Soc. 130*, 1505–1530.

Wedi, N. P. (1999). The numerical coupling of the physical parameters to the dynamical equations in a forecast model. Technical Report 274, Eur. Cent. For Medium-Range Weather Forecasts, Reading, UK.

Wedi, N. P. and P. K. Smolarkiewicz (2004). Extending Gal-Chen & Somerville terrain-following coordinate transformation on time-dependent curvilinear boundaries. *J. Comput. Phys. 193*, 1–20.

Wedi, N. P. and P. K. Smolarkiewicz (2006). Direct numerical simulation of the Plumb-McEwan laboratory analog of the QBO. *J. Atmos. Sci. 63*(12), 3226–3252.

Wedi, N. P. and P. K. Smolarkiewicz (2009). A framework for testing global nonhydrostatic models. *Q.J.R. Meteorol. Soc. 135*, 469–484.

White, A. A. and R. A. Bromley (1995). Dynamically consistent, quasi-hydrostatic equations for global models with a complete representation of the Coriolis force. *Q.J.R. Meteorol. Soc. 121*, 399–418.

Wood, N. and A. Staniforth (2003). The deep-atmosphere Euler equations with a mass-based vertical coordinate. *Q.J.R. Meteorol. Soc. 129*, 1289 – 1300.

Wurtele, M. G., R. D. Sharman, and T. L. Keller (1987). Analysis and simulations of a troposphere - stratosphere gravity wave model. part I. *J. Atmos. Sci. 44*, 32693281.

Yessad, K. (2008). Dynamics. GmapDoc, http://www.cnrm.meteo.fr/gmapdoc/.

Yessad, K. and P. Bénard (1996). Introduction of a local mapping factor in the spectral part of the Météo-France global variable mesh numerical forecast model. *Q.J.R. Meteorol. Soc. 122*, 1701–1719.

A Appendix: An "intermediate" finite-element discretisation in the vertical

A finite-element discretisation for the vertical of the NH model has not been successfully implemented yet, because it leads to an unstable semi-implicit scheme. Nevertheless, the NH model can still benefit in part from the higher computational accuracy of the vertical integrals and derivatives in vertical finite-element (VFE) discretisation based on cubic B-spline elements compared to the vertical finite-difference (VFD) discretisation (cf. Untch and Hortal (2004)) by using the VFE discretisation for selected terms in the explicit part of the model, while performing the semi-implicit computations in VFD discretisation. This "intermediate" VFE discretisation for the NH-IFS is described below.

In the VFE discretisation as implemented in the IFS, discretised analogues of vertical operators are constructed by using the Galerkin method in cubic B-spline space (FE space). The resulting discrete operators (matrices) in FE space are then transformed to physical space (vertical-level space) and used there, cf. Untch and Hortal (2004). In the NH model, both vertical integrals and vertical derivatives have to be evaluated. In contrast, in the hydrostatic IFS with semi-Lagrangian advection only vertical integrals are required, a fact that greatly facilitated the construction of a stable semi-implicit scheme in VFE discretisation for the hydrostatic IFS. The same VFE integral operator computed for the hydrostatic model is also used in the NH model and in addition a VFE derivative operator has been constructed in a similar way (also based on cubic B-splines) by M. Hortal and J. Vivoda. It is noted that this VFE derivative operator is not the exact inverse of the VFE integral operator as in the continuous case. Using the inverse of the VFE integral operator as derivative operator does not give accurate numerical derivatives.

The VFE integral operator is denoted here by $\mathscr{R}_I()_m^l$, where m and l denote the integration limits (i.e. integration from level m to level l). The VFE derivative operator is denoted by $\mathscr{R}_D$.

The terms in the equations (3) and (4) which are discretised with VFE are listed below.

- The integrals in the second and third equation in (4) are discretised as for the hydrostatic VFE model, cf. Untch and Hortal (2004).

- The integral in the first equation in (4) is discretised on model layers l as

$$\Phi_l = \Phi_s + \mathscr{R}_I\left(-\frac{\pi}{p}\frac{RT\delta}{\Delta\eta}\right)_s^l \tag{15}$$

where s denotes the surface. The gradient $\nabla_\eta\Phi$ is discretised as

$$(\nabla_\eta\Phi)_l = \nabla_\eta\Phi_s + \mathscr{R}_I\left(-\Delta\eta^{-1}\left(\frac{\pi}{p}\nabla_\eta(RT)\delta - \frac{\pi}{p}\nabla_\eta\ln\frac{p}{\pi}RT\delta + \frac{\pi}{p}RT\nabla_\eta\delta\right)\right)_s^l \tag{16}$$

Here δ denotes the average pressure depth of a layer, divided by the average pressure of this layer. In NH-IFS $\delta_l = \Delta\pi_l/\pi_l$ is used.

- The pressure gradient term is formulated as

$$\left(\frac{1}{m}\frac{\partial p}{\partial\eta}\nabla_\eta\Phi + RT\frac{\nabla_\eta p}{p}\right)_l = \frac{(\Delta p)_l}{(\Delta\pi)_l}(\nabla_\eta\Phi)_l + (RT)_l(\nabla_\eta\mathscr{2})_l + (RT)_l\left(\frac{\nabla_\eta\pi}{\pi}\right)_l \tag{17}$$

where the computation of $(\Delta p)_l$ requires a vertical derivative in finite-element discretisation as outlined below.

- The term gw is discretised as

$$(gw)_l = gw_s + \mathscr{R}_I \left(-\frac{\pi}{p} \frac{dR_d T \delta}{\Delta \eta} \right)_s^l \tag{18}$$

and it's derivative requires the relation

$$\left(\nabla_\eta \left(\frac{\pi}{p} dR_d T \delta \right) \right)_l = \left(\frac{\pi}{p} \right)_l \left(d_l \delta_l \nabla_\eta (R_d T_l) + R_d T_l \delta_l \nabla_\eta d_l + R_d T_l d_l \nabla_\eta \delta_l \right) + R_d T_l d_l \delta_l \nabla_\eta \left(\frac{\pi}{p} \right)_l. \tag{19}$$

- The total pressure depths needed in the pressure gradient term and in the dw/dt expression for the GWADV-NH option is discretised as

$$(\Delta p)_l = (\Delta \pi)_l \left(\frac{\partial p}{\partial \pi} \right)_l, \tag{20}$$

where

$$\left(\frac{\partial p}{\partial \pi} \right)_l = \frac{p_l}{\pi_l} + \left(\frac{\partial \left(\frac{p - \pi}{\pi} \right)}{\partial \ln \pi} \right)_l \tag{21}$$

with

$$\left(\frac{\partial \left(\frac{p - \pi}{\pi} \right)}{\partial \ln \pi} \right)_l = \mathscr{R}_D \left(\frac{p - \pi}{\pi} \right)_l \frac{(\Delta \eta)_l}{\delta_l}. \tag{22}$$

A VFE discretisation of the remaining explicit terms involving vertical derivatives has also been tried, but resulted in an unstable model. More research is needed to understand why.